

Photon Torpedoes and Rytov Pinwheels: Integral-Equation Modeling of Non-Equilibrium Fluctuation-Induced Forces and Torques on Nanoparticles

M. T. H. Reid,¹ O. D. Miller,² A. G. Polimeridis,³ A. W. Rodriguez,⁴ E. M. Tomlinson,⁵ and S. G. Johnson¹

¹*Department of Mathematics, Massachusetts Institute of Technology, Cambridge, MA 02139*

²*Department of Applied Physics and Energy Sciences Institute, Yale University, New Haven, CT 06511*

³*Skolkovo Institute of Science and Technology, Moscow, Russia*

⁴*Department of Electrical Engineering, Princeton University, Princeton, NJ*

⁵*Department of Physics, Massachusetts Institute of Technology, Cambridge, MA 02139*

(Dated: August 8, 2017)

We present new theoretical tools, based on fluctuational electrodynamics and the integral-equation approach to computational electromagnetism, for numerical modeling of forces and torques on bodies of complex shapes and materials due to emission of thermal radiation out of thermal equilibrium. This extends our recently-developed fluctuating-surface-current (FSC) and fluctuating-volume-current (FVC) techniques for radiative heat transfer to the computation of non-equilibrium fluctuation-induced forces and torques; as we show, the extension is non-trivial due to the significantly greater computational cost of modeling radiative momentum transfer, including a new singularity not present in the energy-transfer case that must be carefully neutralized to yield a tractable solver. We introduce a new analytical cancellation technique that addresses these challenges and allows, for the first time, accurate and efficient prediction of non-equilibrium forces and torques on bodies of essentially arbitrary shapes—including asymmetric and chiral particles—and complex material properties, including continuously-varying and anisotropic dielectrics. We validate our approach by showing that it reproduces known results, then present new numerical predictions of non-equilibrium self-propulsion, self-rotation, and momentum-transfer phenomena in complex geometries that would be difficult or impossible to study with existing methods. Our findings indicate that the fluctuation-induced dynamics of micron-size room-temperature bodies in cold environments involve microscopic length scales but macroscopic time scales, with typical linear and angular velocities on the order of microns/second and radians/second; moreover, for particles of fixed shape we find an optimum particle size at which linear or angular acceleration is maximized. For a micron-scale gear driven by absorption of angular momentum from the thermal radiation of a nearby chiral emitter, we find a strong and non-monotonic dependence of the magnitude and even the *sign* of the induced torque on the temperature of the emitter, suggesting applications to precision nanoscale thermometry.

I. INTRODUCTION

This paper presents new theoretical tools for solving a century-old problem: predicting fluctuation-induced forces and torques on material bodies originating from asymmetric emission of thermal radiation, including thermal self-propulsion/self-rotation (TSP/TSR) of isolated bodies and non-equilibrium (NEQ) Casimir forces/torques between bodies. Although these effects have captured the imagination of scientists and engineers for over a century [1–3] and have been observed in experiments spanning a vast range of length scales—from laboratory measurements of nanofabricated devices [4] to astronomical observations of natural [5] and man-made [6] celestial bodies—the science of *theoretical* modeling of NEQ fluctuation-induced forces and torques has remained in its infancy due to a host of forbidding technical challenges. This may seem surprising in view of rapid recent progress in theoretical methods for the closely related problems of Casimir forces/torques (fluctuation-induced momentum transfer in thermal equilibrium) [7–11] and near-field radiative heat exchange (fluctuation-induced energy transfer out of thermal equilibrium) [12–18]; although results have recently appeared for NEQ forces in geometries involving spheres and/or smooth

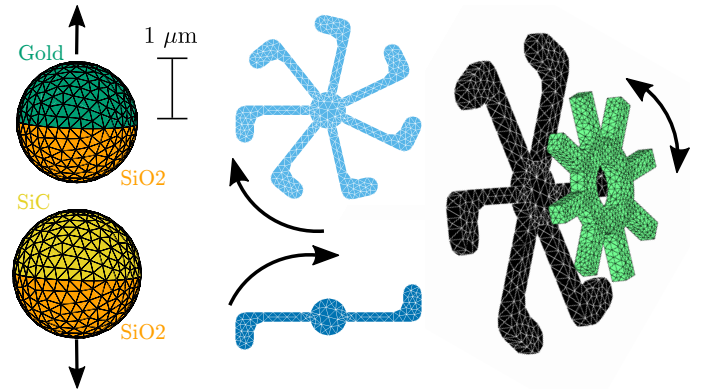


FIG. 1. Synopsis of main results. *Photon torpedoes*: Warm “Janus” particles [19, 20] consisting of conjoined hemispheres of distinct media self-propel in different directions depending on the material combination (Section V A). *Rytov pinwheels*: Warm chiral particles in a cold environment self-rotate counter-clockwise or clockwise depending on the number of pinwheel arms (Section V B). *Non-contact microgears*: A warm Rytov pinwheel causes a nearby gear to spin clockwise or counterclockwise depending on temperature and material combination (Section V C). All structures have linear dimensions on the order of $1 \mu\text{m}$.

or corrugated plates [13, 15, 21–24], we explain below

why the extension to NEQ forces/torques on *arbitrary* bodies is nontrivial, requiring new ideas beyond what is required for equilibrium or heat-transfer problems. A key challenge is the emergence of new divergences that must be carefully neutralized to obtain a tractable numerical method (Section 2). We introduce a new analytical cancellation that solves this problem (Section 3) and present efficient, general-purpose algorithms for accurately predicting TSP/TSR and NEQ forces/torques on bodies of complex shapes and material properties; our tools, which are available as free, open-source software [25, 26], extend both the *fluctuating-surface-current* [27, 28] and *fluctuating-volume-current* [18] approaches to fluctuation-induced interactions, which we previously used to study EQ Casimir forces [29] and NEQ heat transfer [18, 30]. After validating our methods by reproducing known results for non-equilibrium Casimir interactions (Section 4), we use our new tools to obtain numerical predictions of novel fluctuation-induced force and torque phenomena in complicated geometries that would be practically impossible to treat using existing methods (Section 5). Among our findings are that micron-scale asymmetric bodies at room temperature, initially at rest in cold vacuum environments, accelerate while radiatively cooling, ramping up over a time on the order of seconds to terminal linear or angular velocities on the order of microns/second or radians/second; moreover, varying the overall size of fixed-shape particles reveals well-defined optimal sizes for maximal self-thrust.

Thermal and quantum-mechanical fluctuations in material bodies give rise to radiated fields which carry both **(a)** energy and **(b)** momentum to nearby bodies and the surrounding environment [31, 32]. Although mathematical modeling of phenomenon **(a)** dates back to the 19th-century theory of black-body radiation [31] and that of phenomenon **(b)** to the mid-20th century theory of Casimir phenomena [33, 34], recent years have witnessed dramatic advances in the power of theoretical tools to make rigorous predictions of fluctuation-induced phenomena in geometries involving bodies of complex shapes and materials [7–18, 27, 35, 36]. In many cases, these tools—which include both scattering-theoretic methods yielding elegant analytical formulas for high-symmetry geometries [9, 10, 12–16, 35] and fully numerical methods capable of studying arbitrary-shaped bodies [11, 17, 18, 27, 29, 37]—were originally developed to study equilibrium momentum-transfer (Casimir) phenomena [10, 27, 35] and later extended to handle non-equilibrium energy transfer [13, 15, 17, 18].

The further extension to handle non-equilibrium *momentum* transfer would seem a logical next step, and indeed some scattering-matrix methods have been generalized to handle non-equilibrium forces [13, 15, 21–24], and self-propulsion [24] in geometries involving spheres and/or smooth or corrugated plates. However, such studies are relatively few in comparison to the dozens of equilibrium Casimir and heat-transfer geometries that have been investigated by scattering-matrix

methods [8, 10, 12–16, 35, 36, 38, 39]; among the reasons for this may be that the arena in which scattering-matrix methods are most powerful—modeling of high-symmetry bodies—is the maximally uninteresting regime for studies of self-propulsion and self-rotation, which rely crucially on *asymmetry* and vanish for symmetric geometries such as a homogeneous sphere in isolation [21, 24]. In principle, this should be the natural entry point for numerical methods [11] such as finite-difference [37] or integral-equation [27] approaches, which treat all bodies—symmetric or otherwise—on an equal footing and have been used to study EQ-force and heat-transfer problems in complex geometries for which scattering-matrix methods would be unwieldy [11, 40]. However, as discussed in detail below (Section II), the extension of these methods to non-equilibrium momentum-transfer problems turns out to be highly nontrivial due to several complications, including **(a)** rapidly oscillatory functions of position or frequency that pose high costs for numerical integration, and **(b)** a new divergence, stemming ultimately from the fact that electrostatic fields carry momentum but not energy [41], that does not affect EQ-force or heat-transfer problems but must be carefully isolated and cancelled analytically to avoid burying NEQ-force signals in numerical noise.

Our resolution of these difficulties is presented in Section III, where we present fluctuating-surface-current (FSC) and fluctuating-volume-current (FVC) formulas for non-equilibrium momentum exchange among bodies of arbitrary shapes and materials and with their environment. The FSC method, which is based on the surface-integral-equation (SIE) formulation of classical electromagnetic scattering [42–44], originated as a technique for modeling equilibrium Casimir forces between bodies of homogeneous, isotropic material properties [27, 29, 45] and was subsequently extended to describe non-equilibrium heat transfer between such bodies [17, 28]. Later, the FVC approach to heat transfer [18], which is based on the volume-integral-equation (VIE) approach to classical scattering [42–44], was developed as an extension of the FSC paradigm to inhomogeneous and anisotropic bodies.

Although the FSC and FVC techniques differ in their description of currents in material bodies and require completely separate numerical implementations, they share a common conceptual foundation, which was discussed separately for the two cases in Refs. 18, 28 for the specific problem of heat transfer. In Section III A we extend those discussions to more general NEQ-fluctuation problems—including force and torque prediction—using a notation that emphasizes the common structure of the FSC and FVC formulas for fluctuation-induced powers, forces, and torques (PFTs). These formulas involve the traces of products of certain matrices describing the interactions of currents in material bodies; Sections III B and III C respectively discuss the different forms assumed by these matrices in the FVC and FSC cases, and Section III D discusses a crucial analytical cancellation required

in both cases to yield reliable numerical results for NEQ forces and torques. The upshot is a single set of master matrix-trace formulas [equations (14) in Section III E] that may be used to compute fluctuation-induced PFTs in both the FSC and FVC contexts.

An advantage of FSC/FVC methods is that they are agnostic with respect to the choice of basis functions used to describe currents; as discussed in Section III F, there are multiple choices of basis in which to evaluate the matrix-trace formulas (14). For numerical studies of complex, asymmetric geometries, it is convenient to follow common practice in the computer-aided design community [42, 43] by using localized basis functions conforming to a geometry mesh [46, 47]; this is the approach used in all previous FSC and FVC studies [18, 27–29], and we adopt it as our strategy in this paper, using meshed geometries with localized basis functions both to validate our new tools by comparison with known results (Section IV) and to explore novel self-propulsion and self-rotation effects in micron-scale bodies of complex shapes (Section V).

The FSC/FVC approach may be applied to predict fluctuation-induced momentum-transfer phenomena in geometries consisting of any number of bodies. In Section IV we validate our methods by showing that they correctly reproduce known results for non-equilibrium forces between two homogeneous spheres [15]. Thereafter, we focus on the case of individual bodies, using FSC and FVC techniques to obtain new numerical predictions—summarized schematically in Figure 1—for homogeneous and inhomogeneous nanoparticles exhibiting thermal self-propulsion (“photon torpedoes,” Section V A), thermal self-rotation (“Rytov pinwheels,” Section V B), and mechanical actuation mediated by thermal radiation (non-contact thermal microgears, Section V C). We show that the dynamics of these particles involves microscopic length scales but macroscopic time scales: a warm micron-scale asymmetric body placed at rest in a cold environment ramps up to a terminal linear or angular velocity on the order of microns/second or radians/second (Figures 2-4), and varying the overall scale of particles with fixed shapes identifies a optimal size at which thermal self-acceleration is maximized.

The formulas used in this paper to model fluctuation-induced phenomena are implemented in SCUFF-EM [25] and in BUFF-EM [26], free, open-source software implementations of the FSC and FVC approaches to fluctuational electrodynamics.

II. WHY ARE NON-EQUILIBRIUM FORCES AND TORQUES HARD TO COMPUTE?

As noted above, recent years have seen the emergence of sophisticated computational techniques for modeling fluctuation-induced *momentum* exchange *in* thermal equilibrium (Casimir forces/torques) [7, 8, 10, 11] and fluctuation-induced *energy* exchange *out of* equilibrium

(radiative heat transfer) [12–18], spurring predictions of novel EQ Casimir phenomena and NEQ heat-transfer phenomena in a wide variety of complex geometries. In contrast, studies of NEQ forces/torques have been fewer, and have been restricted thus far to relatively high-symmetry geometries—spheres and/or and/or smooth or corrugated plates [13, 15, 21–24]—that admit geometry-specific scattering-matrix treatments [12–16]. Why has it been so difficult to extend existing numerical solvers for fluctuations in general geometries to the problem of NEQ momentum transfers? The goal of this section is to offer a qualitative flavor of the answer to this question, summarizing the computational challenges involved with details relegated to later sections. As we explain, extending existing tools to the problem of NEQ forces in arbitrary geometries is *not* simply a matter of adding an NEQ module to an EQ code, or tacking a force module onto a heat-transfer code; instead, new ideas are required to address unique problems that arise.

At an intuitive level, the greater computational complexity of NEQ forces vs. powers is suggested already by elementary thought experiments. Consider a warm body at uniform temperature T in a cold environment. A simple way to model the energy and momentum lost to thermal radiation is to assume that photons emitted from each infinitesimal surface patch dA carry away energy $dE = \alpha dA$ and momentum $d\mathbf{P} = \frac{\alpha}{c} \hat{\mathbf{n}} dA$ per unit time [41]; here α is a temperature- and material-dependent but position-independent constant, c is the speed of light, and $\hat{\mathbf{n}}$ is the outward-pointing normal to the surface patch. The total rate of energy loss $P = \alpha \int dA = \alpha A$ then scales with surface area, a prediction that captures the correct qualitative behavior [31] and is in quantitative agreement with experimental observations across length scales from the macroscopic to the micron-scale [48], although corrections are required for micron-scale or smaller bodies [49]. On the other hand, the total *momentum* loss per unit time *vanishes* in this simple picture, $-\mathbf{F} = \frac{\alpha}{c} \int_A \hat{\mathbf{n}} dA = 0$, whereupon the *entirety* of the force arises from higher-order corrections; the simple physical model that captures the essential features of radiative energy loss is of no predictive power for the force. (This is for bodies of uniform temperature; in the presence of thermal gradients the naïve picture of normal-directed momentum emission *can* suffice to yield accurate force estimations [6].)

The distinction between power and force here is essentially due to the vector nature of momentum: whereas the *energy* radiation from different regions of a warm body is a scalar quantity that typically adds constructively over the surface, the linear and angular *momentum* emissions vary in direction over the surface and exhibit significant cancellation in many cases, requiring costly fine-grained sampling to resolve numerically [41]. This problem confounds attempts to compute fluctuation-induced forces on bodies by numerically integrating the thermally-averaged Maxwell stress tensor (MST) over bounding surface enclosing the body (Section III a be-

low); cancellations from different surfaces must be carefully resolved, at high computational cost, even as numerical quadrature of the Poynting flux involves little or no cancellation and generally converges rapidly to yield accurate heat-radiation rates [50].

In principle, this difficulty could be overcome simply by sampling the integrand at large numbers of cubature points on the bounding surface [51], and such a brute-force approach is probably tractable for integral-equation approaches to classical, deterministic problems [42, 43]: the MST at each cubature point is a quadratic function of the \mathbf{E} and \mathbf{H} fields there [41], and these in turn are weighted superpositions of the elemental fields radiated by the current distributions of individual basis functions, so the cost of numerical MST integration with N_C cubature points in a geometry with N_{BF} basis functions scales like $O(N_C N_{\text{BF}})$, an inexpensive post-processing step for integral-equation solvers. But things are not so easy for fluctuation-induced phenomena, where we must evaluate the statistical *average* of the MST at each point [32], requiring thermally-averaged products of field components; as discussed below (Section IIIa), the quantities that superpose here are not the fields of individual basis functions but the *products* of fields of individual basis functions, of which—for each cubature point—there are $\sim N_{\text{BF}}^2$. Each additional cubature point thus increases computational cost by an enormous amount proportional to N_{BF}^2 , and the task of resolving delicate MST cancellations by fine-grained sampling quickly becomes intractable.

Of course, surface integration of the MST is not the only way to compute momentum transfer to a body; an equivalent alternative is to consider *volume* integration of the local Lorentz forces [41] on charges and currents in the body (Section IIIb,c below). This technique, which is the basis of the scattering-matrix approach to NEQ forces of Ref. 15, is closely analogous to the technique of computing power transfer by volume-integrating the local Joule heating, as is done in both scattering-matrix approaches [15] and numerical FSC and FVC solvers for NEQ heat transfer [17, 18]. However, in attempting to apply numerical volume-integral methods to calculate forces and torques in arbitrary-shaped bodies, one runs into yet another problematic manifestation of the distinct character of electromagnetic momentum vs. energy transfer—namely, that quasistatic fields produce forces but not power transfer [52]. An obvious example is furnished by two monochromatic (frequency ω) point dipoles, which exert a force on each other that remains finite as $\omega \rightarrow 0$ even as the energy exchange vanishes in that limit [52]. Similarly, a pointlike dipole radiator at a distance d from the surface of a material body transfers energy to the body at a rate that remains finite as $d \rightarrow 0$, but exerts a *force* that *diverges* in this limit due to the contribution of quasistatic fields [41].

It is this latter phenomenon that is troublesome in numerical calculations of fluctuation-induced forces and torques. As described in the following section, our for-

malism computes the fluctuation-induced heating and force on a body essentially by averaging over a thermal ensemble of dipole sources distributed throughout the body, including at points arbitrarily close to the surface—thus yielding the diverging force contributions described above. Physically, these contributions must all *cancel* when integrated over the body to compute the total force, and this cancellation is manifest in theoretical approaches—such as scattering-matrix methods [15]—in which the integrals can be evaluated analytically. However, any finite-resolution numerical code will entail imperfect cancellation of divergent force contributions from different surface regions, yielding numerical noise that dominates the actual signal. For reasons discussed above, this problem is *not* present in numerical heat-transfer solvers [17, 18], which are thus somewhat easier to implement; naïve attempts to repurpose such a code by swapping out Joule heating for Lorentz force in volume integrals are doomed to failure (as we can attest from experience). Instead, as we show in Section IIIb, proper implementation requires careful consideration of the physical requirements of symmetry and reciprocity, which may be exploited to reorganize force and torque calculations in such a way as to achieve *explicit* analytical cancellation of the dangerous terms, yielding an effective numerical method.

Meanwhile, all the complications we have noted thus far arise already in determining the contribution of just a single frequency to the NEQ force/torque; the indefinite sign of momentum transfers creates additional headaches when it comes to evaluating the frequency integrals needed to compute total time averages of fluctuation-induced quantities, which receive contributions from fluctuations on all time scales [32]. Indeed, as has been noted previously [15, 21] and as we illustrate in the examples below (see especially Figure 2), the net momentum emitted or absorbed by a body due to frequency- ω fluctuations may oscillate rapidly with ω , with frequent sign changes and extensive cancellations that can only be resolved by evaluating large numbers of costly integrand samples. This is again in contrast to energy-transfer problems, where the frequency integrand is of definite sign and no cancellations can arise [49]. The upshot is to heighten the urgency of efficient algorithms for computing the force/torque contributions of individual frequencies, as numerical frequency quadratures can easily require hundreds or thousands of samples even for convergence to one or two decimal places (Figure 2).

If fluctuation-induced forces are so difficult to compute, why was it possible for sophisticated computational tools for *equilibrium* Casimir forces to arise over the last decade [7, 10, 27]—tools which, as noted above, predated and laid the groundwork for the current generation of NEQ fluctuation-modeling tools [15–17]? One answer is that for equilibrium problems there is a scalar quantity—the Casimir energy of a configuration of bodies—that may be computed and differentiated with respect to displacement or rotation of the bodies to yield forces and

torques [53]. This strategy is adopted explicitly by many general-purpose equilibrium Casimir methods [10, 11]; moreover, elsewhere we have rigorously demonstrated that the alternative approach of surface-integrating the equilibrium thermal expectation value of the Maxwell stress tensor is exactly equivalent to differentiating an energy expression [27]. A second answer is that, at thermal equilibrium, Wick rotation is available to convert oscillatory real-frequency integrands into smoothly decaying imaginary-frequency integrands of definite sign. [11, 32] This reduces the burden on numerical solvers for EQ problems by allowing accurate estimation of frequency integrals with many fewer integrand samples than is typically required for NEQ force/torque problems. Finally, the simple form of the force law for the zero-temperature Casimir pressure between infinite planar perfect mirrors [34] allows the use of the proximity-force approximation (PFA) [54] to estimate equilibrium forces between closely-spaced bodies, while no such simple approach is available for the NEQ case.

Although we are concerned in this paper with finite-size bodies described by continuum material models, it is interesting to note that the computational problems we have discussed have analogues in the theory of radiative losses from *pointlike* particles [41, 55–57]. For an accelerating pointlike particle, the classical Larmor formula and its relativistic generalization [41] give a straightforward and quantitatively accurate description of the *power* loss, but the accompanying *force* (radiation reaction) on the particle is much more difficult to predict and—despite more than a century of intensive investigation—remains controversial to this day [58, 59]. It is possible that the new theoretical methods we introduce in this paper could shed light on this longstanding problem; we will return to this question in Section VI.

III. FVC/FSC TRACE FORMULAS FOR NON-EQUILIBRIUM FORCES AND TORQUES

The FVC and FSC methods respectively apply techniques borrowed from the volume-integral-equation (VIE) [43] and surface-integral-equation (SIE) [42] approaches to classical scattering to compute rates of fluctuation-induced energy and momentum transfer among material bodies. Special cases of these formulas for the specific case of energy-transfer problems were presented in Refs. 17, 28 for the FSC case and in Ref. 18 for the FVC case; the objective of this section is to extend the FVC and FSC methods to the calculation of general fluctuation-induced quantities—including powers, forces, and torques (PFTs)—and to emphasize the shared conceptual foundations of the two approaches, culminating in a single set of master formulas [Equations (14)] expressing the predictions of both formalisms in a unified language and notation.

The common physical picture underlying FVC and FSC methods attributes fluctuation-induced phenom-

ena to “bare” current fluctuations—in the fluctuation-dissipation sense of Rytov [48]—which are “dressed” by the polarization response of surrounding media, yielding an effective fluctuation-induced source distribution from which PFTs may be computed precisely as in classical, deterministic scattering problems (Section III A). The result is a family of formulas [Equations (14)] expressing spectral densities of PFT contributions as traces of products of matrices, with the various matrices describing the distinct physical ingredients outlined above (bare Rytov currents, material polarization, and PFTs due to sources). Although the particular forms assumed by these matrices differ in the FVC and FSC cases (Sections III B and III C), one feature common to force/torque modeling in *both* frameworks is the need to organize calculations in such a way as to realize a certain analytical cancellation between particular contributions (Section III D)—which, if not properly handled, yield numerical noise that swamps the correct results by several orders of magnitude.

A. Common structure of FSC and FVC trace formulas

Among the various methods available for numerical solution of electromagnetic scattering problems, integral-equation (IE) methods are distinguished by their emphasis on the *sources* of the scattered fields: physical or effective electric and magnetic currents induced by incident fields in the bulk or surface of material bodies [42, 43]. In contrast to other methods (such as the finite-difference [60] or finite-element [61] methods) which solve directly for fields, IE methods typically solve first for induced sources, then compute the scattered fields and other physical quantities of interest—including powers, forces and torques (PFTs)—from the currents as a post-processing step [62, 63]. More specifically, in a deterministic time-harmonic scattering problem at angular frequency ω , let $\mathcal{C}(\mathbf{x})$ be the spatially-varying current distribution induced by incident fields impinging on a body; then the scattered fields are obtained by a linear convolution, $\mathcal{F} \propto \mathcal{G} \star \mathcal{C}$, and the time-average PFTs on the body—which are quadratic functions of the fields—become quadratic forms involving the currents [62, 63]:

$$Q^{\text{PFT}} = \mathcal{C}^* \star \mathcal{Q}^{\text{PFT}} \star \mathcal{C} \quad (\text{deterministic}). \quad (1a)$$

Here $\mathcal{F} = \begin{pmatrix} \mathbf{E} \\ \mathbf{H} \end{pmatrix}$ is the field six-vector, while the current six-vector $\mathcal{C} = \begin{pmatrix} \mathbf{J} \\ \mathbf{M} \end{pmatrix}$ includes both electric currents \mathbf{J} and magnetic currents \mathbf{M} and may be either a volume current distribution existing throughout the bulk of material bodies (for VIE methods [47]) or a surface-tangential current distribution confined to the interfaces between bodies (for SIE methods [46]). The convolution symbol \star correspondingly represents integration over body volumes (VIE) or surfaces (SIE), and \mathcal{G} is the 6×6 dyadic Green’s function (DGF) [43] of the vacuum (VIE) or of

the homogeneous medium in which we are computing the field (SIE). The convolution kernel \mathcal{Q}^{PFT} depends on the formulation and on the quantity being computed; specific expressions are given below. Equation (1a) omits a possible incident-field term that may be present in some scattering problems but is absent for the fluctuational problems considered here; this, and the structure of the \mathcal{Q}^{PFT} operator in SIE and VIE formulations, are discussed briefly in Section III D below and in more detail in Ref. 62.

Numerical IE solvers discretize by approximating the unknown current distribution as an expansion in some convenient discrete set of basis functions,

$$\mathbf{C}(\mathbf{x}) \approx \sum_{\alpha=1}^{N_{\text{BF}}} c_{\alpha} \mathcal{B}_{\alpha}(\mathbf{x}), \quad (1b)$$

where the basis functions $\{\mathcal{B}_{\alpha}\}$ describe volume currents [47] (VIE) or surface currents [46] (SIE). Scattering problems reduce to solving for the N_{BF} -dimensional vector \mathbf{c} of current coefficients [43], after which time-average PFT quantities are computed as vector-matrix-vector products [64],

$$\mathcal{Q}^{\text{PFT}} = \mathbf{c}^{\dagger} \mathcal{Q}^{\text{PFT}} \mathbf{c} = \text{Tr} \left[\mathcal{Q}^{\text{PFT}} \mathbf{c} \mathbf{c}^{\dagger} \right] \quad (\text{deterministic}) \quad (1c)$$

where \mathcal{Q}^{PFT} is the $N_{\text{BF}} \times N_{\text{BF}}$ matrix of the operator \mathcal{Q}^{PFT} in the $\{\mathcal{B}_{\alpha}\}$ basis. (For reasons that will be clear shortly, we have here rewritten the vector-matrix-vector product as the trace of a matrix product involving the rank-one outer-product matrix $\mathbf{c} \mathbf{c}^{\dagger}$.)

The emphasis on sources makes IE methods particularly well-suited to the study of Casimir forces and other fluctuation-induced phenomena, which arise from thermal and quantum-mechanical fluctuations of the currents \mathbf{C} in material bodies [32]. The stochastic nature of these currents ensures a vanishing mean value $\langle \mathbf{C} \rangle = 0$ for any individual current component, but *products* of current components in lossy bodies may have nonvanishing thermal averages, prescribed by fluctuation-dissipation theorem in the form of Rytov [48]:

$$\left\langle \mathcal{C}_{\mu}^{\text{free}}(\mathbf{x}) \mathcal{C}_{\nu}^{\text{free}*}(\mathbf{x}') \right\rangle_{\omega} = \mathcal{R}_{\mu\nu}(\mathbf{x}) \delta(\mathbf{x} - \mathbf{x}'), \quad (1d)$$

$$\mathcal{R}(\mathbf{x}) \equiv \frac{2k \mathcal{Z}_0^{-1}}{\pi} \Theta(T(\mathbf{x}, \omega)) \text{Im} \mathcal{X}(\mathbf{x}),$$

$$\Theta(T, \omega) = \hbar\omega \left[\frac{1}{e^{\hbar\omega/kT} - 1} + \frac{1}{2} \right],$$

where $\mathcal{X} = \begin{pmatrix} \epsilon^{-1} & 0 \\ 0 & \mu^{-1} \end{pmatrix}$ is the spatially-varying material susceptibility tensor and $\mathcal{Z}_0 = \begin{pmatrix} Z_0 & 0 \\ 0 & Z_0^{-1} \end{pmatrix}$ with $Z_0 \approx 377 \Omega$ the impedance of vacuum. [Here and below, the symbols “Re” and “Im” applied to matrices denote Hermitian symmetrizing and anti-symmetrizing *matrix* (not elementwise) operations.] Thus quadratic functions of currents—such as the time-average PFT quantities in (1a) and (1c)—may have nonzero thermal averages, whose values are readily computed in the IE framework.

The superscript on \mathcal{C} in (1d) indicates that the right-hand side of that equation is to be interpreted as the mean-square amplitude of a “free” current distribution $\mathcal{C}^{\text{free}}(\mathbf{x})$ embedded in the surface or volume of a material body. The *total* current contributing to PFTs in (1a) includes both $\mathcal{C}^{\text{free}}$ and the *induced* current \mathcal{C}^{ind} resulting from the polarization response of the body to $\mathcal{C}^{\text{free}}$; in linear media—our exclusive focus in this paper—the total current may be represented as a linear convolution of the form [48, 52]

$$\mathbf{C} = \mathcal{C}^{\text{free}} + \mathcal{C}^{\text{ind}} = \mathcal{W} \star \mathcal{C}^{\text{free}} \quad (1e)$$

where we have introduced the symbol \mathcal{W} to denote a certain linear operator—depending through \mathcal{X} on the material geometry and discussed in more detail below—which “dresses” the bare distribution $\mathcal{C}^{\text{free}}$ to yield the total current including the polarization response of the material bodies. For example, at low frequencies the \mathcal{W} operator for a homogeneous dielectric sphere reduces to a simple multiplicative factor, $\mathcal{W}^{\epsilon\text{-sphere}} \xrightarrow{\omega \rightarrow 0} \frac{3}{(2+\epsilon)}$.

Using \mathcal{W} to “dress” the bare Rytov source distribution (1d) now yields the correlation function of the full current distribution in (1a),

$$\langle \mathbf{C} \mathbf{C}^* \rangle_{\omega} = \mathcal{W} \star \mathcal{R} \star \mathcal{W}^{\dagger},$$

or, in terms of the discretized representation (1c),

$$\langle \mathbf{c} \mathbf{c}^{\dagger} \rangle_{\omega} = \underbrace{\mathbf{W} \mathbf{R} \mathbf{W}^{\dagger}}_{\mathbf{D}} \quad (1f)$$

where \mathbf{R} and \mathbf{W} are the matrix representations of \mathcal{R} and \mathcal{W} and convolutions have become matrix multiplications; we refer to \mathbf{R} and \mathbf{D} here as the “Rytov” and “dressed Rytov” matrices, with the latter describing the bare Rytov distribution as “dressed” by the polarization response of the material geometry. Then the thermally-averaged PFT (1c) reads

$$\begin{aligned} \langle \mathcal{Q}^{\text{PFT}} \rangle_{\omega} &= \text{Tr} \left[\mathcal{Q}^{\text{PFT}} \langle \mathbf{c} \mathbf{c}^{\dagger} \rangle_{\omega} \right] \\ &= \text{Tr} \left[\mathcal{Q}^{\text{PFT}} \mathbf{W} \mathbf{R} \mathbf{W}^{\dagger} \right] \quad (\text{fluctuational}). \end{aligned} \quad (1g)$$

Equation (1h) is the fluctuational analogue of the deterministic formula (1c); in particular, the matrix \mathcal{Q}^{PFT} is the *same* matrix in both cases, and the formulas differ only in that the rank-one matrix $\mathbf{c} \mathbf{c}^{\dagger}$ describing deterministic currents in (1c) is replaced by the *full*-rank matrix $\mathbf{D} = \mathbf{W} \mathbf{R} \mathbf{W}^{\dagger}$ describing the effective mean-square distribution of fluctuation-induced currents contributing to PFTs.

Equation (1g) gives the spectral density of PFT contributions arising from source fluctuations at frequency ω ; the full thermally-averaged PFT then follows by accounting for the contributions of all frequencies,

$$\langle \mathcal{Q}^{\text{PFT}} \rangle = \int_0^{\infty} \langle \mathcal{Q}^{\text{PFT}} \rangle_{\omega} d\omega. \quad (1h)$$

The logical sequence of physical ideas leading from (1a) to (1g) goes through equally well in both VIE and SIE frameworks and for any choice of basis functions; all that differs are the particular forms assumed by the \mathbf{Q} , \mathbf{R} , and \mathbf{W} matrices. In following two sections we discuss the computation of the \mathbf{R} and \mathbf{W} matrices in the FVC and FSC frameworks, while in Section III D we discuss computation of the \mathbf{Q} matrices in both frameworks.

B. Non-equilibrium forces and torques in the VIE context: The FVC force and torque formulas

In VIE solvers [43, 44], $\mathbf{C} = \begin{pmatrix} \mathbf{J} \\ \mathbf{M} \end{pmatrix}$ is a six-vector volume current distribution whose magnetic components \mathbf{M} vanish for non-magnetic media ($\mu = 1$). The induced portion of this current, $\mathbf{C}^{\text{ind}}(\mathbf{x})$, is typically nonzero at any point \mathbf{x} inside a material body, where it is linearly related to the total electromagnetic fields at \mathbf{x} through a 6×6 susceptibility tensor \mathcal{X} [65]:

$$\mathbf{C}^{\text{ind}}(\mathbf{x}) = -ik\mathbf{Z}_0^{-1}\mathcal{X}(\mathbf{x})\mathcal{F}^{\text{tot}}(\mathbf{x}) \quad (2)$$

$$k = \frac{\omega}{c}, \quad \mathcal{X} = \begin{pmatrix} \epsilon^{-1} & 0 \\ 0 & \mu^{-1} \end{pmatrix}, \quad \mathbf{Z}_0 \equiv \begin{pmatrix} Z_0 & 0 \\ 0 & Z_0^{-1} \end{pmatrix}$$

[For non-magnetic media ($\mu = 1$) this reduces to simply $\mathbf{J} = -i\omega\epsilon_0(\epsilon - 1)\mathbf{E}^{\text{tot}}$ with $\mathbf{1}$ the 3×3 identity matrix.] To derive an expression for the dressing matrix \mathbf{W} , we take \mathcal{F}^{tot} to be the field radiated by the bare current \mathbf{C}^{free} plus the field of the corresponding induced current, i.e.

$$\mathbf{C}^{\text{ind}} = k^2\mathcal{X}\left[\mathcal{G}^0 \star (\mathbf{C}^{\text{free}} + \mathbf{C}^{\text{ind}})\right] \quad (3)$$

with \mathcal{G}^0 the 6×6 vacuum Green's dyadic, related to the usual 3×3 and scalar Green's functions [9, 66, 67] by

$$\mathcal{G}^0 \equiv \begin{pmatrix} \mathbb{G}^0 & \mathbb{C}^0 \\ -\mathbb{C}^0 & \mathbb{G}^0 \end{pmatrix} \quad (4a)$$

$$\mathbb{G}_{ij}^0(\mathbf{r}) = \left[\delta_{ij} + \frac{1}{k^2}\partial_i\partial_j \right] \frac{e^{ik|\mathbf{r}|}}{4\pi|\mathbf{r}|} \quad (4b)$$

$$= \frac{e^{ikr}}{4\pi k^2 r^3} \left[f_1(ikr)\delta_{ij} + f_2(ikr)\frac{r_i r_j}{r^2} \right], \quad (4c)$$

$$\mathbb{C}_{ij}^0(\mathbf{r}) = -\frac{1}{ik}\epsilon_{ijk}\partial_k\mathbb{G}_{k\ell}^0 \quad (4d)$$

$$= \frac{e^{ikr}}{4\pi(ik)r^3} f_3(ikr)\epsilon_{ijk}r_k, \quad (4e)$$

$$f_1(x) \equiv -1+x-x^2, \quad f_2(x) \equiv 3-3x+x^2, \quad f_3(x) \equiv -1+x.$$

Using (3) to compute the total current $\mathbf{C} = \mathbf{C}^{\text{free}} + \mathbf{C}^{\text{ind}}$ yields an expression for the “dressing” operator \mathbf{W} in (1e):

$$\mathbf{W} \equiv \mathbf{1} + (\mathbf{1} - k^2\mathcal{X}\mathcal{G}^0)^{-1}.$$

For a given basis of expansion functions $\{\mathcal{B}_\alpha\}$, the matrix of the \mathbf{W} operator may be related to the matrices of the \mathcal{X} and \mathcal{G}^0 operators according to

$$\mathbf{W} = \left[\mathbf{1} + \mathbf{S}^{-1}\mathbf{V}\mathbf{S}^{-1}\mathbf{G}^0 \right]^{-1} \quad (5)$$

where the various matrices have elements

$$S_{\alpha\beta} = \langle \mathcal{B}_\alpha | \mathcal{B}_\beta \rangle, \quad (6a)$$

$$V_{\alpha\beta} = -k^2 \langle \mathcal{B}_\alpha | \mathcal{X} | \mathcal{B}_\beta \rangle, \quad (6b)$$

$$G_{\alpha\beta}^0 = \langle \mathcal{B}_\alpha | \mathcal{G}^0 | \mathcal{B}_\beta \rangle. \quad (6c)$$

(The notation \mathbf{V} for the matrix of the quantity $-k^2\mathcal{X}$ follows Refs. 10, 15, where this quantity is interpreted as a scattering-theoretic “potential.”) Similarly, the matrix of the Rytov operator \mathcal{R} [Equation (1d)] describing the fluctuation-induced free source distribution dressed by \mathbf{W} has elements

$$R_{\alpha\beta} = \frac{2k}{\pi} \langle \mathcal{B}_\alpha | \mathbf{Z}_0^{-1} \Theta \text{Im } \mathcal{X} | \mathcal{B}_\beta \rangle. \quad (6d)$$

The task of a numerical [26] FVC solver is then simply to evaluate, for an appropriate set of volume-current basis functions $\{\mathcal{B}_\alpha\}$, the numerical integrals [68] defining the matrix elements (6), then evaluate the matrix-product trace in (1g) via standard methods of numerical linear algebra [69].

Equation (5) may be derived from equation (3) by expanding \mathbf{C}^{ind} and \mathbf{C}^{free} via (1b) and using the completeness relation [70]

$$\sum_{\alpha\beta} S_{\alpha\beta}^{-1} \mathcal{B}_{\alpha\mu}^*(\mathbf{x})\mathcal{B}_{\beta\nu}(\mathbf{x}') = \delta_{\mu\nu}\delta(\mathbf{x} - \mathbf{x}'). \quad (7)$$

For a finite basis set—such as the SWG [47] functions used for the FVC computations of Section V A in which the number of basis functions is proportional to the number of tetrahedra into which objects are discretized—equation (7) is only an approximate equality, with the approximation improving as the basis set is refined [70].

C. Non-equilibrium forces and torques in the SIE context: The FSC force and torque formulas

In SIE solvers, $\mathbf{C}(\mathbf{x}) = \begin{pmatrix} \mathbf{K} \\ \mathbf{N} \end{pmatrix}$ is an effective tangential *surface* current distribution localized on interfaces between homogeneous material regions. Although the basic logical sequence leading to equation (1g) remains unchanged in this case—PFT quantities are quadratic functions of currents, thermal averages of current-current products are related to temperatures and susceptibilities by fluctuation-dissipation relations, and assembling these ingredients yields trace formulae of the form (1g)—the physical interpretation of \mathbf{C} is now subtly different. One immediate clue is the fact that the magnetic surface current \mathbf{N} is generally nonzero even for non-magnetic media.

As this observation demonstrates, the surface currents in SIE solvers do not coincide with the physical sources of the scattered fields; instead, \mathbf{C} is properly understood as a tally of boundary data recording the total tangential \mathbf{E} and \mathbf{H} fields present at material interfaces [71, 72].

Despite this shift in viewpoint, it remains straightforward to write SIE versions of equations like (1a) and (1c) expressing PFT quantities in classical deterministic problems as quadratic functions of the effective surface currents [62]. On the other hand, the derivation of appropriate bare and dressed Rytov matrices \mathbf{R} and \mathbf{D} for use in (1g) is more subtle, as it is not obvious how one translates the Rytov correlation function (11d) for physical volume currents into a statement about effective surface currents. Nonetheless, as shown in Ref. 28, in the SIE context it remains possible to write down a \mathbf{D} matrix appropriate for use in equation (1g): for PFTs induced by sources in body s among a collection of one or more homogeneous bodies, the matrix

$$\mathbf{D} = -\frac{4}{\pi}\Theta(T_s, \omega)\mathbf{M}^{-1}\left(\text{sym } \mathbf{G}^s\right)\mathbf{M}^{-1\dagger} \quad (8)$$

plays a role equivalent to that of \mathbf{WRW}^\dagger in (1g). Here T_s is the temperature of the source body (assumed constant throughout the body) and \mathbf{M} is the discretized SIE matrix for the collection of objects (which enters classical scattering problems through a relation of the form $\mathbf{M}\mathbf{c} = \mathbf{v}$ with \mathbf{v} the basis-set projection of the incident field); for a single homogeneous body, \mathbf{M} is just the sum of the matrix representations, in the $\{\mathcal{B}_\alpha\}$ basis, of the Green’s dyadics for the material media exterior and interior to the body, $M_{\alpha\beta} = \langle \mathcal{B}_\alpha | \mathcal{G}^{\text{ext}} + \mathcal{G}^{\text{int}} | \mathcal{B}_\beta \rangle$. [72]. The matrix $(\text{sym } \mathbf{G}^s)$ in (8) is a symmetrized version of the portion of \mathbf{M} that describes the self-interactions of surface currents on body s , retaining only the contributions of the medium interior to that body.

The structure of equation (8) is similar to that of (1f); in both cases we have a matrix describing *bare* source fluctuations (\mathbf{R} or $\text{sym } \mathbf{G}^s$) that is conjugated (“dressed”) by a matrix describing the polarization response of surrounding media (\mathbf{W} or \mathbf{M}^{-1}) to yield a matrix (\mathbf{D}) describing the full (physical volume or effective surface) thermal current distribution, which may be paired with various \mathbf{Q}^{PFT} matrices to compute various fluctuation-induced PFT quantities.

However, a key difference between SIE and VIE is that the VIE formulation for material bodies in vacuum or a homogeneous, isotropic background medium refers only to the dyadic Green’s function \mathcal{G}^0 of the background medium, for which closed-form analytic expressions are available; this is true *irrespective* of the complexity of the material properties of the bodies, which may—for example—be anisotropic or continuously spatially varying without requiring any modification of the VIE solution procedure. In contrast, the SIE formulation requires knowledge of the Green’s functions for the media both exterior *and* interior to the scattering bodies; in practice, this restricts FSC methods to problems involving only

bodies of homogeneous, isotropic permittivity and permeability and homogeneous temperature. For VIE there is no such limitation, so the FVC method is the appropriate choice for bodies with inhomogeneous temperature distributions or continuously varying or anisotropic material properties.

D. Methods for writing \mathbf{Q}^{PFT} matrices: Analytical cancellation of numerical divergences

The PFT trace formula (1f) involves two ingredients: the dressed Rytov matrix \mathbf{D} , discussed in the previous two sections, which describes thermal current fluctuations as dressed by the electromagnetic response of surrounding media, and the \mathbf{Q}^{PFT} matrix, describing the power, force, and torque on bodies as a quadratic function of the currents. Whereas the derivation of the \mathbf{D} matrix relies on quantum-statistical-mechanical reasoning as embedded in the Rytov correlation function (1d), the \mathbf{Q} matrix involves strictly classical, deterministic considerations. Elsewhere we have presented detailed discussions of the structure of the classical \mathbf{Q} matrices in the IE [62] framework; as discussed in that reference, for each PFT quantity there are in fact multiple *distinct* methods for writing \mathbf{Q} matrices, all equivalent in exact arithmetic and with complete basis sets, but differing in accuracy and efficiency for practical numerical computations. In many classical scattering problems, the various approaches are somewhat interchangeable, offering similar computational cost and accuracy; for fluctuational problems, on the other hand, one particular strategy emerges as the clear favorite, as we now discuss.

To compute the absorbed power or force on a body, one may evaluate either (a) a surface integral [50, 73], involving the Poynting vector (PV) or Maxwell stress tensor (MST), over the body surface or over a closed bounding surface surrounding but displaced from the body [the “displaced-surface-integral PFT” (DSIPFT) approach], or (b) a volume integral [15], involving the local Joule heating $\frac{1}{2}\text{Re } \mathcal{C}^\dagger \mathcal{F}$ or Lorentz force $\frac{1}{2\omega}\text{Im } \mathcal{C}^\dagger \nabla \mathcal{F}$ inside the body. The latter case further bifurcates according as we relate \mathcal{C} to \mathcal{F} using equation (2)—the “overlap PFT” (OPFT) approach, so called because the \mathbf{Q} matrix elements in this case involve overlap integrals between basis functions—or using the convolution $\mathcal{F} = \mathcal{G} \star \mathcal{C}$, which we term the “energy-momentum transfer PFT” (EMTPFT) approach because PFTs in this case may be interpreted as transfers of energy or momentum from incident fields to currents [62]. (In the SIE case, the OPFT may alternatively be derived by collapsing the bounding surface of the DSIPFT approach to the body surface and expressing the PV or MST in terms of surface currents [62].)

In principle we thus have three distinct algorithms—DSIPFT, EMTPFT, or OPFT—for computing \mathbf{Q}^{PFT} matrices. However, the OPFT approach—while computationally the most efficient method, and one which generally yields acceptable accuracy in deterministic

problems—turns out to be unsuitable for force and torque calculations in fluctuational settings, for reasons discussed in Ref. 62. On the other hand, the DSIPFT approach typically yields good accuracy in both deterministic and fluctuational problems, but—though cost-competitive with other methods in the deterministic case—is prohibitively expensive for fluctuational calculations. Briefly, the reason is that computing each element of the \mathbf{Q} matrix involves a costly individual numerical cubature over the bounding surface; for the rank-one calculation of equation (1c) the calculation may be rearranged to avoid explicitly forming \mathbf{Q} , but for the full-rank problem of equation (1g) there is no bypassing the time-consuming evaluation of \mathbf{Q} elements.

This leaves the EMTPFT strategy as the only viable option for accurate and efficient evaluation of fluctuation-induced forces and torques in both the SIE and VIE frameworks. Here we briefly sketch the essentials of this approach.

In EMTPFT we identify the power absorption, force, and torque on a body with the energy, linear momentum, and angular momentum transferred to currents in the body—either physical volume currents in the VIE case, or effective surface currents in the SIE case—by the ambient fields. Thus, in a VIE solver the power [18, 63], force and torque on a body may be computed as volume integrals of the form

$$\mathbf{P} = \frac{1}{2} \text{Re} \int_V \mathbf{C}^* \mathcal{F} dV \quad (9a)$$

$$\mathbf{F} = \frac{1}{2\omega} \text{Im} \int_V \mathbf{C}^* \nabla \mathcal{F} dV \quad (9b)$$

$$\mathcal{T} = \frac{1}{2\omega} \text{Im} \int_V \underbrace{\{\mathbf{C}^* \times \mathcal{F} + \mathbf{C}^* (\mathbf{r} \times \nabla) \mathcal{F}\}}_{\mathbf{C}^* \tilde{\nabla} \mathcal{F}} dV \quad (9c)$$

The symbol $\tilde{\nabla}$ for the operator defined by (9c) is a convenient shorthand notation for torque calculations.

The VIE power formula (9a) was discussed extensively in the classical scattering context in Ref. 63 and in the radiative heat-transfer context in Ref. 18; the latter reference also quoted the force formula (9b), but omitted details. Equations (9b,c) are intuitively reminiscent of the expressions $\mathbf{p} \cdot \nabla \mathbf{E}$ and $\mathbf{p} \times \mathbf{E}$ for the force and torque on a point dipole in an external electrostatic field [41]; they may be derived rigorously by considering the usual Lorentz force on the charges and currents in an infinitesimal volume and applying Maxwell's equations and Stokes' theorem to the volume integral.

When \mathcal{F} in (9) is the field radiated by \mathbf{C} itself—a situation encountered when computing the self-force or self-torque on a body due to thermal fluctuations within it—the force reads

$$F_i = \frac{1}{2c} \text{Im} \iint \left(\begin{array}{c} \mathbf{J} \\ \mathbf{M} \end{array} \right)^\dagger \left(\begin{array}{cc} iZ_0 \partial_i \mathbb{G}^0 & i \partial_i \mathbb{C}^0 \\ -i \partial_i \mathbb{C}^0 & iZ_0^{-1} \partial_i \mathbb{G}^0 \end{array} \right) \left(\begin{array}{c} \mathbf{J} \\ \mathbf{M} \end{array} \right) d^2V \quad (10)$$

with $\mathbb{G}^0, \mathbb{C}^0$ the dyadic Green's functions of vacuum (or the embedding medium), Equation (4). Although equa-

tion (10) would appear to define a *singular* integral in view of the short-distance singularities of the kernels (4) [e.g. $\mathbb{G}^0(\mathbf{r}) \sim \frac{1}{|\mathbf{r}|^3}$ as $|\mathbf{r}| \rightarrow 0$], this appearance is misleading; upon rearranging and exploiting the reciprocity relations $\{\mathbb{G}^0, \mathbb{C}^0\}_{ij}(\mathbf{r}) = \{\mathbb{G}^0, \mathbb{C}^0\}_{ji}(-\mathbf{r})$ one finds that singular terms in the integrand explicitly cancel in (10), yielding an expression of the form

$$F_i = \frac{1}{2c} \iint \left\{ \text{Im} \left(Z_0 J_j^* J_k + Z_0^{-1} M_j^* M_k \right) \text{Im} \partial_i \mathbb{G}_{jk}^0 - \text{Re} \left(J_j^* M_k - M_j^* J_k \right) \text{Re} \partial_i \mathbb{C}_{jk}^0 \right\} d^2V \quad (11)$$

involving only the nonsingular operators $\text{Im} \mathbb{G}^0$ and $\text{Re} \mathbb{C}^0$, which behave for small \mathbf{r} like [9, 67]

$$\text{Im} \mathbb{G}_{ij}^0(\mathbf{r}) = \frac{k}{6\pi} \delta_{ij} - \frac{k^3 r^2}{30\pi} \left[\delta_{ij} - \frac{1}{2} \frac{r_i r_j}{r^2} \right] + O(r^4) \quad (12a)$$

$$\text{Re} \mathbb{C}_{ij}^0(\mathbf{r}) = \left[\frac{-k^2}{12\pi} + \frac{k^4 r^2}{120\pi} + O(r^4) \right] \varepsilon_{ijk} r_k. \quad (12b)$$

Note that our derivation of (11) used only the reciprocity of the *exterior* medium, not that of the scatterer, and thus remains valid for non-reciprocal scatterers.

Analogous manipulations of the power and torque formulas (9a,c) show that the contributions of singular operator terms cancel from these integrals as well; discretizing according to (1b) then yields trace formulas (1c) for the power and i -directed force and torque with elements of the $\mathbf{Q}^{\text{P,F,T}}$ matrices involving inner products of volume-current basis functions with the nonsingular operators $\text{Im} \mathbb{G}^0, \text{Re} \mathbb{C}^0$ and their derivatives:

$$Q_{\alpha\beta}^{\text{P}} = \frac{\omega}{2c} \left\langle \mathcal{B}_\alpha \left| \begin{pmatrix} Z_0 \text{Im} \mathbb{G}^0 & -\text{Re} \mathbb{C}^0 \\ +\text{Re} \mathbb{C}^0 & +Z_0^{-1} \text{Im} \mathbb{G}^0 \end{pmatrix} \right| \mathcal{B}_\beta \right\rangle, \quad (13a)$$

$$Q_{\alpha\beta}^{\text{F}_i} = \frac{1}{2c} \left\langle \mathcal{B}_\alpha \left| \begin{pmatrix} Z_0 \text{Im} \partial_i \mathbb{G}^0 & -\text{Re} \partial_i \mathbb{C}^0 \\ +\text{Re} \partial_i \mathbb{C}^0 & +Z_0^{-1} \text{Im} \partial_i \mathbb{G}^0 \end{pmatrix} \right| \mathcal{B}_\beta \right\rangle, \quad (13b)$$

$$Q_{\alpha\beta}^{\text{T}_i} = \frac{1}{2c} \left\langle \mathcal{B}_\alpha \left| \begin{pmatrix} Z_0 \text{Im} \tilde{\partial}_i \mathbb{G}^0 & -\text{Re} \tilde{\partial}_i \mathbb{C}^0 \\ +\text{Re} \tilde{\partial}_i \mathbb{C}^0 & +Z_0^{-1} \text{Im} \tilde{\partial}_i \mathbb{G}^0 \end{pmatrix} \right| \mathcal{B}_\beta \right\rangle \quad (13c)$$

Here $\tilde{\partial}_i$ denotes the i th component of the operator $\tilde{\nabla}$ defined by (9c).

Equations (9) and (13) are for the VIE case. The SIE case is closely analogous, with (a) the volume integrals in (9) replaced by surface integrals; (b) the current \mathbf{C} now understood to represent effective (equivalence-principle) electric and magnetic surface currents instead of physical volume currents; (c) the matrix elements (13) now involving 4-dimensional integrals over surface basis functions instead of 6-dimensional integrals over volume basis functions; (d) the vacuum dyadics $\mathbb{G}^0, \mathbb{C}^0$ replaced by the dyadic Green's functions for the homogeneous medium exterior to the body (if it is not vacuum). These retain

the nonsingular limiting forms (12) *as long as the exterior medium is lossless* (so that k is real-valued), but exhibit short-distance singularities in lossy exterior media that invalidate EMTPFT force and torque (but not power [28]) calculations in that case—a state of affairs that is hardly unexpected given the murky status of electromagnetic momentum (but not power [74]) in lossy media [52].

The explicit reciprocity-enabled cancellation of the singular contributions to (10) affords a major reduction in the computational cost of EMTPFT calculations, as the integrals (13) defining \mathbf{Q} -matrix elements—whose computation typically dominates the cost—are now *nonsingular* and may be evaluated by simple numerical cubature [51], obviating the need for complicated and expensive techniques for evaluating singular integrals [62, 68]. For *power* computations, this speedup is convenient but inessential; the singular contributions to \mathbf{Q}^P -matrix elements cancel harmlessly out of numerical evaluations of (1g), and their retention degrades efficiency but not accuracy.

For *force* and *torque* computations, on the other hand, the cancellation of singular contributions effected by the transition from (10) to (11) is not just a computational convenience, but a crucial ingredient in establishing a tractable numerical algorithm. The difficulty is that the most singular contributions to (10)—specifically, the contributions associated with the $\frac{1}{|\mathbf{r}|^3}$ terms in $\mathbb{G}_0(\mathbf{r}), \mathbb{C}_0(\mathbf{r})$ —describe force contributions that are essentially electrostatic in nature, and the integral (10) effectively sums force contributions between pairs of electrostatic dipoles separated by arbitrarily short distances d , yielding force contributions diverging like $\sim d^{-4}$ [41]. Physically these contributions must all cancel, and this cancellation occurs naturally when the integral is evaluated analytically as is done in scattering-matrix approaches [15]. But naïve discretization of (10) using localized basis functions—such as the piecewise-linear tetrahedron-based SWG functions [47] or triangle-based RWG functions [46] we use below (Sections IV, V)—destroys the exact cancellation, resulting in overwhelming numerical noise swamping the signal in equation (10). (We emphasize again that this disease does not afflict power computations, as there is no power exchange between electrostatic dipoles [41].) Thus the exact cancellation that converts (10) into (11) is not merely an optional computational acceleration, but rather an essential ingredient required for any tractable numerical implementation of the FSC/FVC approach to non-equilibrium force and torque computation.

E. Master FSC/FVC formulas for non-equilibrium PFTs

Assembling the ingredients from the preceding sections, we obtain the following master formulas for the spectral density at frequency ω of contributions to pow-

ers, forces, and torques in both FSC and FVC contexts:

$$\langle P \rangle_\omega = \text{Tr} \left[\mathbf{Q}^P \text{Re} (\mathbf{WRW}^\dagger) \right] \quad (14a)$$

$$\langle F_i \rangle_\omega = \text{Tr} \left[\mathbf{Q}^{F_i} \text{Im} (\mathbf{WRW}^\dagger) \right] \quad (14b)$$

$$\langle \mathcal{T}_i \rangle_\omega = \text{Tr} \left[\mathbf{Q}^{\mathcal{T}_i} \text{Im} (\mathbf{WRW}^\dagger) \right] \quad (14c)$$

As discussed above, the \mathbf{Q} matrices in these formulas—whose entries are inner products of surface- or volume-current basis functions with desingularized dyadic Green’s functions and their derivatives, Eq. (13)—describe the PFT contributions of pairs of unit-amplitude basis functions, while the dressed Rytov matrices $\mathbf{D} = \mathbf{WRW}^\dagger$ describe the mean-square amplitudes of fluctuation-induced currents as dressed by the polarization response of the material geometry. In the following sections we use SIE and VIE implementations of these formulas to predict new nonequilibrium force and torque phenomena in nanoparticle systems.

The fact that the power formula in (14) involves $\text{Re } \mathbf{D}$, while the force and torque formulas involve $\text{Im } \mathbf{D}$, may be traced back to (a) the Re and Im operators in the volume-integral expressions for power and for force/torque in Eq. (9), together with (b) the fact that the \mathbf{Q}^P matrix in (13) is symmetric, while \mathbf{Q}^F and \mathbf{Q}^T are antisymmetric.

The *dimension* of the matrix traces in (14) is the total number of basis functions used to represent volume or surface currents in the material geometry; for the discretized-mesh-conforming localized basis functions we choose here (discussed in the following section), the number of basis functions required to achieve reasonable accuracy is on the order of a few hundred to a few thousand.

F. Choice of basis functions

The FVC and FSC formulas presented above are agnostic with respect to the choice of basis functions $\mathcal{B}_\alpha(\mathbf{x})$ used to represent current distributions [equation (1b)]. In practice, many choices of basis function are available, with the appropriate selection dictated by the needs of the problem at hand.

For numerical calculations involving objects of complicated shapes, it is convenient to follow the practice of discretized integral-equation solvers in computational engineering [42], by using *localized* basis functions describing elemental current distributions confined within geometric regions of specific shapes (triangles, tetrahedra, cubes, etc.) Bodies of complex shapes may be approximated to arbitrary desired accuracy as unions of these shapes (see insets of Figures 3 and 6) and the accuracy with which the current distribution is represented may be systematically improved, at cost of greater computational expense, by refining the sizes of the elements. Common examples include (a) RWG basis functions for

surface currents [46], which are localized in triangles on discretized surface meshes such as the mesh of Figure 6; (b) SWG basis functions for volume currents [47], which are localized over tetrahedra in discretized volume meshes such as the mesh of Figure 3; and (c) piecewise-constant basis functions for volume currents [63], which may be defined on uniformly-spaced voxel grids to allow efficient FFT-based convolutions. (RWG and SWG functions are named for their inventors [46, 47].)

The numerical calculations reported in this paper were obtained using localized basis functions (RWG and SWG functions for SIE and VIE methods, respectively). All calculations were performed using SCUFF-EM [25] or BUFF-EM [26], both of which are free, open-source software packages available for download online.

IV. VALIDATION

Before using our new tools to predict new fluctuation-induced interactions in previously-unexplored geometries (Section V), we first validate our methods by demonstrating that they reproduce the results of Ref. 15 for the non-equilibrium Casimir force between homogeneous spheres—among the few existing theoretical results for momentum transfer between compact bodies out of thermal equilibrium.

We consider homogeneous spheres of radius $R = 100$ nm separated by a distance of $d=6$ μm along the z axis (sphere 2 lies above sphere 1). The spheres are composed of gold, whose material properties at the infrared frequencies relevant for thermal radiation are adequately described by a Drude-type dielectric function [15]:

$$\epsilon^{\text{gold}}(\omega) = 1 - \frac{\omega_p^2}{\omega(\omega + i\gamma)} \quad (15)$$

with $\{\omega_p, \gamma\} = \{1.37 \cdot 10^{16}, 5.32 \cdot 10^{13}\}$ rad/sec. The contribution of fluctuations in sphere s to the total z -directed force on sphere d ($s, d \in \{1, 2\}$) is given by

$$F_{s \rightarrow d} = \int_0^\infty \Theta(T_s, \omega) \Phi_{s \rightarrow d}^{\text{Force}}(\omega) d\omega \quad (16)$$

where T_s is the temperature of sphere s (assumed constant throughout the sphere) and the temperature-independent force “flux” Φ^{Force} may be computed using analytical formulas given in Ref. 15 or numerically using FSC/FVC methods: putting $Q = F_z$ in equation (1g), we have $\Phi^{\text{Force}} = \langle F_z \rangle / \Theta(T_s, \omega)$. The power transfer from sphere s to sphere d is given by (16) with Φ^{Force} replaced by the power flux Φ^{Power} .

Figure 2 plots $\phi_{1 \rightarrow 2}^{\text{Force}}$ (upper) and $\phi_{2 \rightarrow 2}^{\text{Force}}$ (lower) and as computed using the numerical FSC solver SCUFF-EM [25] (circles) and using the analytical formulas of Ref. 15 (solid lines). For comparison, we also plot $\phi_{1 \rightarrow 2}^{\text{Power}}$ (inset of upper plot). Red (blue) circles/lines denote positive (negative) quantities, with positive force data corresponding to repulsive forces. The sphere surfaces are

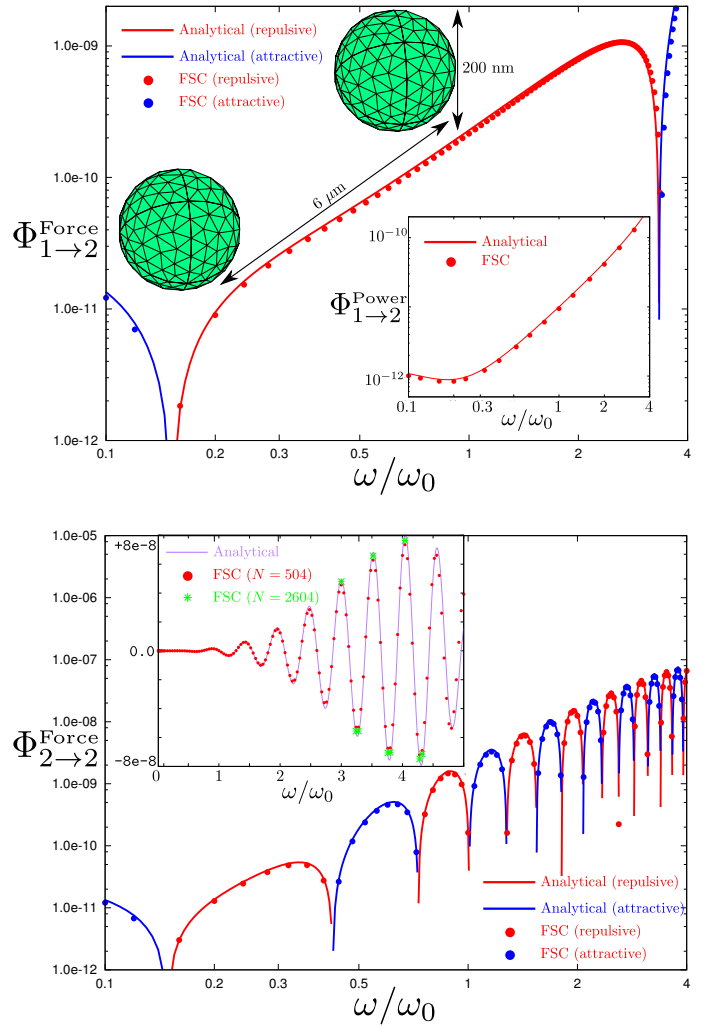


FIG. 2. Frequency dependence of fluctuation-induced energy and momentum flux between gold nanospheres of radius 100 nm separated by a center-center distance of 6 μm . Solid lines indicate predictions of the analytical T -matrix formulas of Ref. 15. Filled circles denote FSC calculations for sphere surface meshes with $N = 504$ triangle edges (inset, not to scale). Green stars in the inset of the lower plot denote FSC calculations with finer surface meshes ($N = 2604$). *Upper plot*: Flux (see text) of force on sphere 2 due to radiation from sphere 1. *Upper plot inset*: Flux of power into sphere 2 due to radiation from sphere 1. *Lower plot*: Flux of force on sphere 2 due to its own radiation, graphed on log-log (main plot) and linear-linear (inset) scales. Whereas the power flux is always positive and gently varying with frequency, the force flux may be positive or negative (attractive or repulsive) depending on the frequency, with the self-force flux $\phi_{2 \rightarrow 2}^{\text{force}}$ in particular exhibiting rapid oscillations. The need to resolve these oscillations accurately when integrating over frequency makes force calculations significantly more costly than heat-transfer calculations. *Units*: Frequency is measured in $\omega_0 = 3 \cdot 10^{14}$ rad/sec. Power fluxes ϕ^{Power} have units of watts / $\hbar\omega_0^2$. Force fluxes ϕ^{Force} have units of nanoNewtons / $\hbar\omega_0^2$. Note that the quantities plotted here are temperature-independent *fluxes*, which must be weighted by the Bose-Einstein factor $\Theta(T, \omega)$ and integrated over frequency to yield actual rates of energy and momentum transfer at a given temperature T .

discretized into unions of flat triangular panels (upper inset) with $N_{\text{edge}} = 504$ total triangle edges per sphere; the total number of surface-current basis functions is $4N_{\text{edge}}$ (electric and magnetic currents on both spheres), so the dimension of the matrices in (1g) is $N_{\text{BF}} = 2016$.

The agreement between numerical FSC data and the analytical formulas is evidently excellent for all quantities at all frequencies. In particular, the FSC results accurately capture the rapid oscillations of $\Phi_{2 \rightarrow 2}^{\text{Force}}(\omega)$ (main plot in lower panel), which Ref. 15 attributed to constructive/destructive interference between waves emitted by sphere 2 and their reflections from sphere 1. Closer scrutiny of the data on a linear-linear scale (inset of lower panel) reveal slight discrepancies between FSC and analytical data near peaks and troughs of the oscillation; these are due to finite meshing resolution and are reduced by repeating FSC calculations with spheres meshed at the finer resolution of $N_{\text{edge}} = 2604$ interior edges (green stars in lower inset), corresponding to matrices of dimension $N_{\text{BF}} = 8256$ in (1g).

Beyond validating the methods proposed in this paper, Figure 2 lends intuition to the discussion of Section II regarding the greater computational cost of force calculations as compared to power calculations. The force integrand in (16) exhibits sign changes for both the $1 \rightarrow 2$ and $2 \rightarrow 2$ cases—with particularly violent oscillations in the latter case—requiring large numbers of integrand samples, each involving costly evaluation of the matrix-trace formulas (1g), to yield accurate numerical estimates of the total integrated force. In contrast, the power integrand (inset of upper plot) is always positive and varies slowly with frequency, allowing the frequency integral to be evaluated at modest computational cost.

V. APPLICATIONS

A. The photon torpedo: Self-propulsion of warm inhomogeneous nanoparticles in a cold environment

Figure 3 plots, as a function of temperature, the self-propulsion force on various hybrid particles designed to realize the notion of a “photon torpedo.” The idea is to surround a mass of homogeneous, thermally radiating material—silicon dioxide in this case—with a *partial* reflective coating; for example, one might consider replacing the lower hemisphere of a $1 \mu\text{m}$ -radius SiO_2 sphere with a metallic substance (inset). Then thermally-emitted photons radiated in the direction of the lower hemisphere are reflected by the metallic region, ensuring a net upward-directed stream of momentum carried away by the thermally-emitted photons; to conserve momentum, the particle must *recoil* in the downward direction—that is, the direction of the reflective coating. Micron-scale “Janus” particles of this sort may be readily fabricated via standard techniques and are a focus of current interest in nanophotonics research [19, 20]; here we explore their non-equilibrium self-propulsion properties.

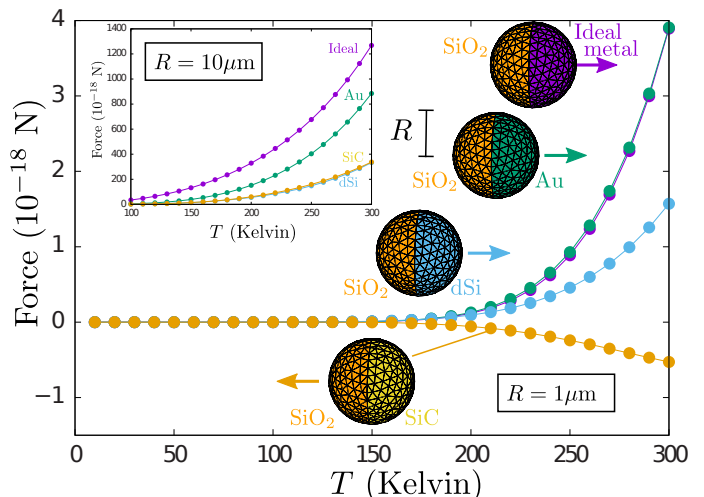


FIG. 3. Thermal self-propulsion of warm (temperature T) “photon torpedoes” in a cold (0 K) environment. The torpedoes are “Janus” particles [19] consisting of SiO_2 spheres of radius R with one full hemisphere replaced by an impostor substance: ideal plasmonic metal (purple), real gold (green), doped silicon (cyan), or silicon carbide (yellow). Simple arguments (see text) suggest that the self-propulsion force experienced by the particle should be directed toward the impostor hemisphere; for particles of radius $R = 1 \mu\text{m}$ (main figure), this prediction is borne out for the three metallic impostor substances, but the SiO_2 - SiC particle self-propels in the opposite direction (lowermost curve in main plot). This phenomenon reverses itself for larger particles with $R = 10 \mu\text{m}$ (inset); now the force is directed toward the impostor region for all material combinations. The magnitude of the force is on the order of 10^{-18} N for the $1 \mu\text{m}$ particles and scales roughly with the volume of the particle, increasing approximately 1,000 fold for $10 \mu\text{m}$ -radius particles.

In Figure 3 we have investigated this concept for Janus particles of radius $R = \{1, 10\} \mu\text{m}$ consisting of an SiO_2 hemisphere paired with hemispheres of various materials: **(a)** an idealized lossless metal (purple) described by the plasmonic dielectric function

$$\epsilon^{\text{ideal metal}}(\omega) = 1 - \left(\frac{\omega_p}{\omega}\right)^2$$

with $\omega_p = 3 \cdot 10^{16}$ rad/sec; **(b)** real gold (Au) (green) with the dielectric function of Eq. (15), **(c)** doped silicon (dSi) (cyan), and **(d)** silicon carbide (SiC) (yellow). The figure plots the magnitude and sign of the self-propulsion force experienced by the Janus particle versus its temperature T in a background environment maintained at $T = 0$ K. For the three metallic substances, the particle experiences a self-propulsion force directed toward the metallic hemisphere in keeping with the intuitive prediction of the photon-torpedo picture; this is true both for particles of radius $R = 1 \mu\text{m}$ (main figure) and for larger particles with $R = 10 \mu\text{m}$ (inset). On the other hand, the behavior is more subtle when the metallic material is replaced by the dielectric insulator SiC: now the force is directed

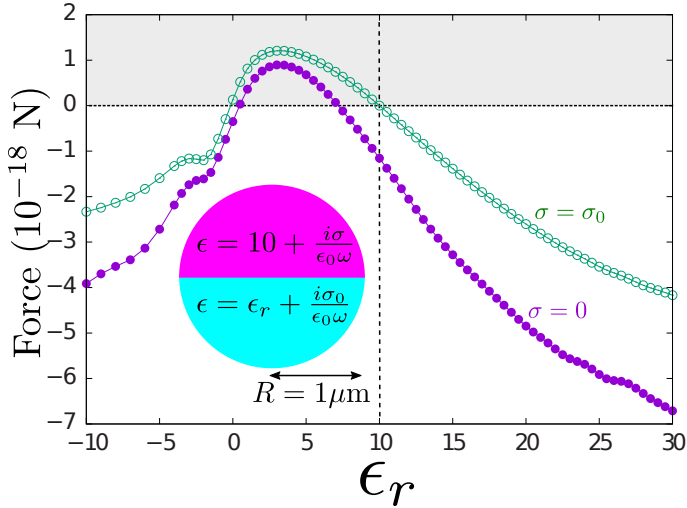


FIG. 4. Self-propulsion vs. dielectric contrast of warm (300 K) Janus particle in 0K background. The conductivity of the lower hemisphere is fixed at $\sigma_0 = (Z_0 \cdot 1 \mu\text{m})$, while the real part of its relative dielectric constant varies over the range $\epsilon_r \in [-30, 10]$. The upper hemisphere has real relative dielectric constant fixed at 10 and either vanishing conductivity (filled purple circles) or conductivity σ_0 (hollow green circles). By symmetry the force on the particle must vanish when the upper and lower media are identical (intersection of dashed lines), but for other media combinations the magnitude and sign of the force vary in non-intuitive ways.

toward the SiO_2 hemisphere (that is, opposite the direction expected for a “photon torpedo” and observed for the metallic hemispheres) for $R = 1 \mu\text{m}$ particles, but toward the SiC hemisphere (i.e. in the “torpedo-like” direction) for $R = 10 \mu\text{m}$.

The difficulty of predicting the sign of thermal-propulsion forces is further illustrated by Figure 4, in which we have plotted the self-propulsion force of a 300K Janus particle in a 0K background as a function of the dielectric contrast between upper and lower hemispheres. The lower hemisphere has relative permittivity $\epsilon = \epsilon_r + \frac{i\sigma_0}{\epsilon_0\omega}$ with conductivity fixed at $\sigma_0 = (Z_0 \cdot 1 \mu\text{m})^{-1}$ and varying real part ϵ_r . The upper hemisphere has fixed real relative dielectric constant 10 and conductivity $\sigma = 0$ (purple) or σ_0 (green). The self-propulsion force vanishes by symmetry when the upper and lower hemispheres are identical (intersection of dashed lines); for other values of the dielectric contrast it is difficult to predict the magnitude and even the *sign* of the force.

We conclude that the design of self-propelling nanoparticles is subtle; heuristic design intuition may prevail in some cases, but reliable predictions require rigorous numerical tools like those presented in this paper.

Terminal velocities. A particle of temperature T^P released into an environment of temperature T^{env} will eventually equilibrate through (among other mechanisms) the emission or absorption of thermal radiation. Neglecting conductive and convective heat transfer, the temporal

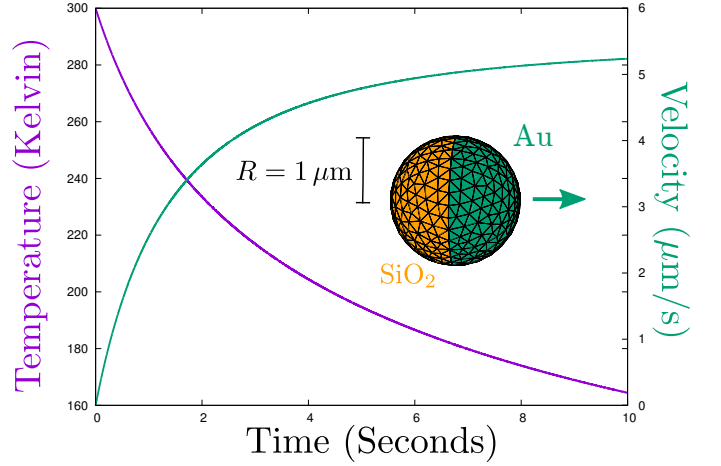


FIG. 5. Temporal evolution of the temperature (purple) and velocity (green) on a $1\text{-}\mu\text{m}$ gold- SiO_2 Janus-particle photon torpedo heated to a temperature of 300 K and released into a cold (0K) environment. The torpedo ramps up to a terminal linear velocity of $\sim 5 \mu\text{m/s}$ over an interval of ~ 10 s.

evolution of the particle temperature is given by

$$\frac{dT}{dt} = -\frac{1}{\kappa}H(T) \quad (17a)$$

with κ the heat capacity and $H = \frac{dU}{dt}$ the temperature-dependent rate of energy emission/absorption due to thermal radiation. Solving (17a) with boundary condition $T(t=0) = T^P$ yields a function $T(t)$ describing the time evolution of the particle temperature; at the equilibration time t^* defined by $T(t^*) = T^{\text{env}}$ the particle has exhausted its “fuel” and thereafter exhibits no net radiative exchange of energy or momentum with the medium. Neglecting drag forces and other dissipative effects, the particle then remains in motion at fixed linear and angular velocities $\{\mathbf{v}, \boldsymbol{\omega}\}^{\text{terminal}}$ given by

$$\mathbf{v}^{\text{terminal}} = \frac{1}{m} \int_0^{t^*} \mathbf{F}(T(t)) dt \quad (17b)$$

$$\boldsymbol{\omega}^{\text{terminal}} = \frac{1}{I} \int_0^{t^*} \boldsymbol{\mathcal{T}}(T(t)) dt \quad (17c)$$

with m, I the particle mass and moment of inertia. The temperature-dependent rates of energy and momentum exchange $\{H, \mathbf{F}, \boldsymbol{\mathcal{T}}\}(T)$ may be computed for arbitrary particles using the methods discussed in Section II, and we may use this information to determine the temperature trajectory $T(t)$ and compute the terminal velocities of warm nanoparticles released into vacuum. Figure 5 shows the time-varying temperature (purple curve) and velocity (green curve) of the gold- SiO_2 Janus-particle photon torpedo of Figure 3, assuming a heat capacity of $\kappa=800 \text{ J/(kg K)}$ [15] an average mass density of $\rho \approx 3 \text{ g/cm}^3$, and an environment temperature $T^{\text{env}} = 0 \text{ K}$.

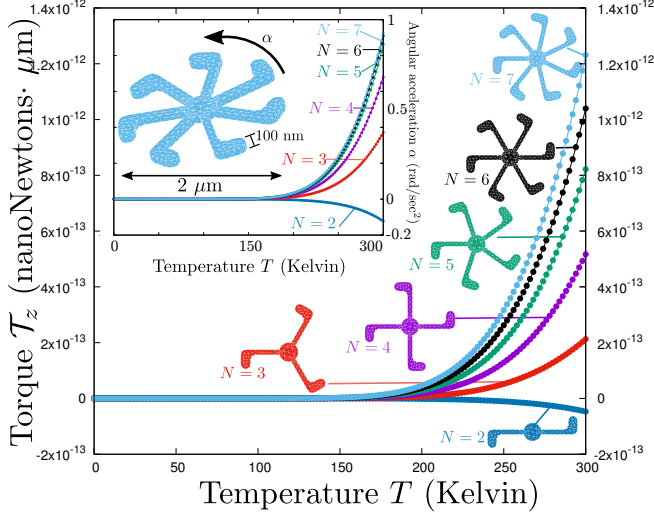


FIG. 6. Thermal self-rotation of Rytov pinwheels in a cold environment. *Main figure:* Self-rotation torque \mathcal{T}_z vs. pinwheel temperature T . The magnitude of the torque at $T=300$ K grows steadily with the number of pinwheel arms N , increasing by roughly a factor of 4 as N varies from 2 to 7. *Inset:* Angular acceleration $\alpha = \mathcal{T}_z/I_z$ with I_z the moment of inertia about the z axis. Now all curves approximately collapse onto a single universal trajectory, yielding a macroscopic angular acceleration of ~ 0.05 rad/sec² at 300 K. Increased font size of inset axis labels.

The torpedo ramps up to a terminal linear velocity of ~ 5 $\mu\text{m/s}$ over an interval of ~ 10 s.

Dynamics on microscopic length scales but macroscopic time scales. A curious feature of the self-propulsion dynamics of warm micron-size bodies is the coexistence of microscopic length scales with macroscopic time scales. Indeed, forces on the order of 10^{-19} Newtons acting on particles of mass on the order of 10^{-14} kg yield accelerations on the order of 10 $\mu\text{m/s}^2$. An experimentalist observing the resulting motion through a microscope could view or video-record the trajectories in real time.

Order-of-magnitude comparisons of force and acceleration mechanisms. For micron-scale particles at 300 K in 0K backgrounds, the self-propulsion forces of Figures 3-5 are on the order of $\sim 10^{-20}$ N, yielding accelerations on the order of ~ 1 $\mu\text{m/s}$. By comparison, typical forces felt by micron-scale particles in laser optical traps are on the order of $\sim 10^{-12} - 10^{-10}$ N [75, 76], while the gravitational acceleration at the Earth’s surface is ~ 10 m/s.

B. The Rytov pinwheel: Self-rotation of warm chiral nanoparticles in a cold environment

Figure 6 plots the self-rotation torque \mathcal{T}_z experienced by chiral nanoparticles—“Rytov pinwheels”—of various

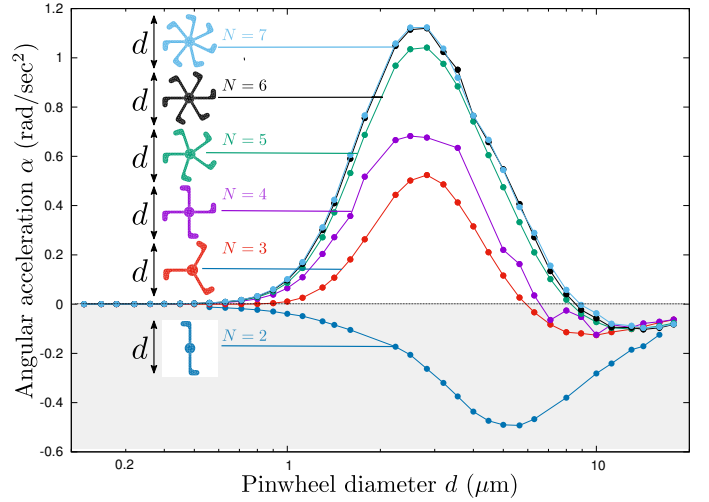


FIG. 7. Angular acceleration $\alpha = \mathcal{T}_z/I_z$ vs. diameter d for warm ($T = 300\text{K}$) gold pinwheels with various numbers of arms N in a cold ($T = 0$ K) environment. For all N we find an optimal diameter $d^{\text{opt}} \in [2, 6]\mu\text{m}$ at which the acceleration is maximized. For $N = 2$ the acceleration is negative (pinwheel spins clockwise as seen looking into the page) for all diameters d . For $3 \leq N \leq 7$ the acceleration is positive (pinwheel spins counter-clockwise) for diameters near d^{opt} but reverses sign for larger d .

temperatures T in a cold (0K) environment. The pinwheels consist of gold sheets of thickness 100 nm etched into the shape of a central disc from which emanate $N = \{2, 3, 4, 5, 6, 7\}$ arms extending to an outer radius of 1 μm —an object that could be fabricated by standard lithographic and etching techniques. The net loss of angular momentum due to the asymmetric polarization of thermal radiation imparts to the pinwheel a recoil torque whose magnitude grows steadily with N (main figure), increasing nearly sixfold as N varies over the range [3, 7]. Interestingly, the $N = 2$ pinwheel exhibits self-rotation in the direction opposite that of all other pinwheels.

Dividing by the moment of inertia $I_z = \int_V (x^2 + y^2)\rho dV$ to yield values of the angular acceleration $\alpha = \mathcal{T}_z/I_z$ collapses the $N = \{5, 6, 7\}$ curves onto a single trajectory, with the $N = 4$ case also falling within $\sim 20\%$ (inset). This suggests the existence of a limiting angular acceleration attained by self-rotating chiral particles in the $\mathcal{I}_z \rightarrow \infty$ limit.

How does this limiting self-acceleration vary with the absolute size of a particle of fixed shape and aspect ratio? Figure 7 plots angular acceleration vs. pinwheel diameter for pinwheels at fixed temperature $T = 300$ K in a 0 K environment; the diameter- d pinwheel with N arms is simply the N -arm pinwheel of Figure 6 with all linear dimensions scaled uniformly by $d/2\mu\text{m}$ so that aspect ratios are preserved (in particular, the ratio of thickness to diameter remains fixed at $1/20$, as in the upper inset of Figure 6.) For all values of N we find a well-defined optimum particle diameter in the range $d^{\text{opt}} \in [2, 6]\mu\text{m}$

at which self-acceleration is maximized. (The value of d^{opt} shifts to larger values as the pinwheel temperature decreases.)

As in Figure 6, for most values of d the $N = 2$ pinwheel self-rotates in the direction opposite that of the $N > 2$ pinwheels; this is true in particular for particles at or near the optimal diameter d^{opt} . On the other hand, as d increases beyond d^{opt} the self-acceleration of the $N = 3$ and higher pinwheels decreases in magnitude and eventually changes sign, so that for $d \gtrsim 8 \mu\text{m}$ all pinwheels join the $N = 2$ case in rotating counter-clockwise. Partial insight into this curious phenomenon is afforded by considering the (deterministic) angular-momentum absorption profile of the pinwheels under irradiation by a circularly-polarized beam (see Figure and discussion below).

Like the photon torpedo, the self-rotation dynamics of the Rytov pinwheel merge microscopic length scales with macroscopic time scales: these micron-scale bodies spin at human-scale angular frequencies on the order of ~ 1 rad/sec, motions readily observable under a microscope in real time.

C. The non-contact thermal microgear: Temperature-dependent sign of angular-momentum transfer between warm and cold bodies

Can the angular momentum radiated by a warm chiral body be captured by a nearby cold body to induce rotation? Figure 8 plots the angular acceleration of a cold (0 K) gold microgear, positioned at various (center-center) distances d above the $N = 6$ pinwheel of Figure 6, as a function of the pinwheel temperature T in a cold (0 K) environment. Like the pinwheel, the microgear is etched from a $1\text{-}\mu\text{m}$ thick sheet of gold; its outer radius is approximately $6 \mu\text{m}$. The torque exhibits a surprising non-monotonic temperature dependence, reversing sign at a d -independent temperature near $T = 160$ K. Although the magnitude of the torque is largest at small gear-pinwheel separation distance $d = 3 \mu\text{m}$, the sign-reversal effect persists at all separation distances considered, including separations as large as $d = 18 \mu\text{m}$ (inset).

The origins of the temperature-dependent sign of this *fluctuation-induced* torque may be understood by considering the angular-momentum absorption profile of the gear in a *deterministic* setting. Figure 9 plots the torque on the isolated gear irradiated by a circularly-polarized plane wave $\mathbf{E}^{\text{inc}}(\mathbf{x}) = \frac{E_0}{\sqrt{2}}(\hat{\mathbf{x}} + i\hat{\mathbf{y}})e^{i\omega z/c}$ with $E_0 = 1$ V / μm . In this figure, the purple curve shows the rate of angular momentum (AM) absorption (radiation torque) for the isolated microgear illuminated by a circularly-polarized plane wave (lower inset) vs. the plane-wave angular frequency ω , measured in units of $\omega_0 = 3 \cdot 10^{14}$ rad/sec. There exists a frequency window in the range $1.5\omega_0 < \omega < 2\omega_0$ within which the gear extracts angular momentum of the opposite sign from the polarization of the bare plane wave. The blue and green curves show

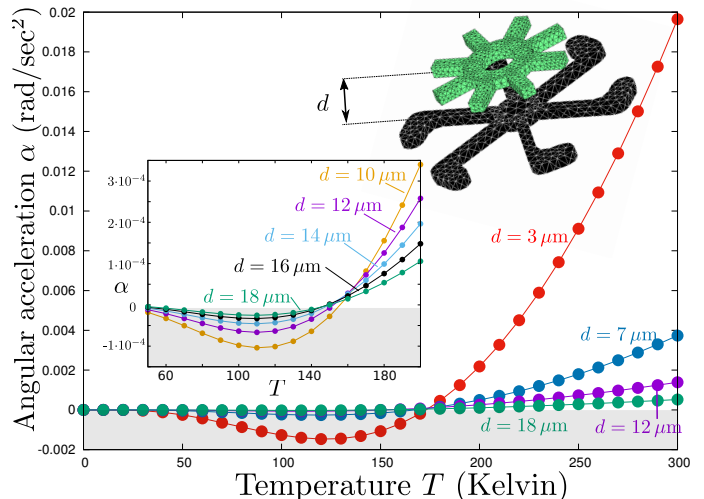


FIG. 8. Torque on a cold (0 K) gold microgear induced by absorption of angular momentum from thermal radiation emitted by the $N = 6$ Rytov pinwheel of Figure 6 at various pinwheel temperatures T in a cold (0 K) environment. The torque exhibits an unexpected change in sign at a pinwheel temperature near $T = 160$ K. Although the magnitude of the torque is greatest at the smallest gear-pinwheel separation distance of $d = 3 \mu\text{m}$, the sign-reversal effect persists even at much greater distances (inset). Increased font size of axis labels.

the spectral density of angular momentum carried away by thermal radiation from an isolated $N = 6$ Rytov pinwheel (upper inset) at pinwheel temperatures $T = 125$ K (green) and $T = 300$ K (blue). [This is just the negative of the integrand in (1g) for the pinwheel self-torque.] Depending on the temperature of the pinwheel, the gear's window of opposite-sign angular-momentum absorption is or is not substantially excited, yielding the strongly temperature-dependent torque of Figure 8.

VI. CONCLUSIONS

The subtle, intuition-confounding behavior on display in Figures 3, 7, and 8 testifies to the need for rigorous quantitative approaches to the modeling of non-equilibrium fluctuation-induced interactions. In contrast to equilibrium Casimir phenomena—for which simple pictures such as the proximity-force approximation (PFA) [54] suffice in many cases (though certainly not all [77]) to lend qualitatively correct insight, and simple approximations such as the leading terms in scattering-theoretic series expansions often suffice to capture key qualitative features [78]—the intricate nature of non-equilibrium phenomena often invalidates naïve intuitive approaches and demands the full power of the unique new computational apparatus we have supplied. Indeed,

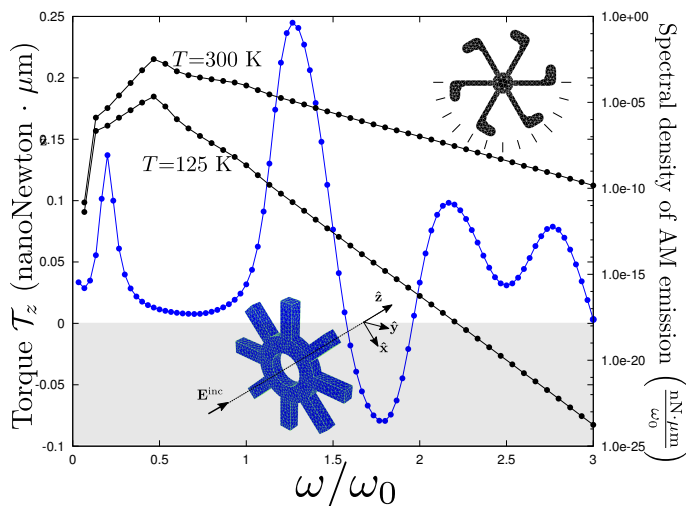


FIG. 9. Elucidating the mechanism of the temperature-dependent sign of the torque in Figure 8. The purple curve shows the rate of angular momentum (AM) absorption (radiation torque) for the isolated microgear illuminated by a circularly-polarized plane wave (lower inset) vs. the plane-wave angular frequency ω , measured in units of $\omega_0 = 3 \cdot 10^{14}$ rad/sec. There exists a frequency window in the range $1.5\omega_0 < \omega < 2\omega_0$ within which the gear extracts angular momentum of the opposite sign from the polarization of the bare plane wave. The blue and green curves show the spectral density of angular momentum carried away by thermal radiation from an isolated $N = 6$ Rytov pinwheel (upper inset) at pinwheel temperatures $T=125$ K (green) and $T=300$ K (blue). Depending on the temperature of the pinwheel, the gear’s window of opposite-sign angular-momentum absorption is or is not substantially excited, yielding the strongly temperature-dependent torque of Figure 8.

it is difficult to imagine how the answers even to binary questions such as the direction of self-propulsion for the photon torpedoes of Figure (3), or the sign of the torque for the Rytov pinwheels of Figures (6) and (7), could have

been predicted with *any* confidence based on *a priori* intuition or back-of-envelope estimates—nor addressed with any existing paradigm for predicting non-equilibrium interactions. Of course, perhaps with time the various novel phenomena predicted by our numerical tools will lend themselves to new sorts of intuitive pictures, and new PFA-like approaches to nonequilibrium forces and torques will arise; we hope the efficient new algorithms we have presented here, together with our free, open-source software implementations [25, 26], will be of service in speeding the arrival of this new understanding.

It is interesting to note that the characteristic motion of micron-scale self-propelling and self-rotating particles involves microscopic length scales but macroscopic time scales; typical linear accelerations and terminal velocities are on the order of microns/second² and microns/second, while typical terminal angular velocities are on the order of radians per second. An experimentalist observing or filming these particles through a microscope would be able to follow their trajectories in real time.

In a different vein, we noted in Section II that one of the problems tackled in this paper—the self-force on a macroscopic, continuum dielectric body resulting from its own radiation—has a microscopic analogue in the well-known problem of the radiative reaction force felt by an accelerating *pointlike* particle [57–59]. Theoretical approaches to this problem [41, 55] often proceed by effectively discretizing a finite-volume model of an accelerating particle and writing equations similar to our equation (10) to estimate radiative reaction force. However, to our knowledge all previous studies of this sort have been *analytical* efforts based on hand calculation, for which restrictive approximations such as rigidity and spherical symmetry—limiting consideration to nonrelativistic motion—are mandatory to render progress tractable. It may be of interest to apply a version of the formalism we have developed here—perhaps with localized basis functions and meshed geometries capable of faithfully capturing particle shape distortions in relativistic motion—to rigorous numerical studies of radiation reaction beyond the non-relativistic regime.

-
- [1] W. Crookes, Philosophical Transactions of the Royal Society of London **164**, 501 (1874).
 - [2] D. P. Rubincam and S. J. Paddack, Science **316**, 211 (2007).
 - [3] G. Beekman, Journal for the History of Astronomy **37**, 71 (2006), <http://jha.sagepub.com/content/37/1/71.full.pdf+html>.
 - [4] M. Liu, T. Zentgraf, Y. Liu, G. Bartal, and X. Zhang, Nature nanotechnology **5**, 570 (2010).
 - [5] M. Kaasalainen, J. Durech, B. D. Warner, Y. N. Krugly, and N. M. Gaftonyuk, Nature **446**, 420 (2007).
 - [6] S. G. Turyshv, V. T. Toth, G. Kinsella, S.-C. Lee, S. M. Lok, and J. Ellis, Phys. Rev. Lett. **108**, 241101 (2012).
 - [7] A. Lambrecht, P. A. M. Neto, and S. Reynaud, New Journal of Physics **8**, 243 (2006).
 - [8] K. A. Milton and J. Wagner, Journal of Physics A: Mathematical and Theoretical **41**, 155402 (2008).
 - [9] S. Scheel and S. Yoshi Buhmann, Acta Physica Slovaca **58**, 675 (2008).
 - [10] S. J. Rahi, T. Emig, N. Graham, R. L. Jaffe, and M. Kardar, Phys. Rev. D **80**, 085021 (2009).
 - [11] S. G. Johnson, in *Casimir Physics*, Lecture Notes in Physics, Vol. 834, edited by D. Dalvit, P. Milonni, D. Roberts, and F. da Rosa (Springer, Berlin, 2011) Chap. 6, pp. 175–218, arXiv:1007.0966.
 - [12] A. Narayanaswamy and G. Chen, Phys. Rev. B **77**, 075125 (2008).
 - [13] R. Messina and M. Antezza, Phys. Rev. A **84**, 042102 (2011).
 - [14] C. Otey and S. Fan, Phys. Rev. B **84**, 245431 (2011).

- [15] M. Krüger, G. Bimonte, T. Emig, and M. Kardar, *Phys. Rev. B* **86**, 115423 (2012).
- [16] J. Lussange, R. Guérout, F. S. S. Rosa, J.-J. Greffet, A. Lambrecht, and S. Reynaud, *Phys. Rev. B* **86**, 085432 (2012).
- [17] A. W. Rodriguez, M. T. H. Reid, and S. G. Johnson, *Phys. Rev. B* **86**, 220302 (2012).
- [18] A. G. Polimeridis, M. T. H. Reid, W. Jin, S. G. Johnson, J. K. White, and A. W. Rodriguez, *Phys. Rev. B* **92**, 134202 (2015).
- [19] A. Walther and A. H. E. Mller, *Chemical Reviews* **113**, 5194 (2013), pMID: 23557169, <http://dx.doi.org/10.1021/cr300089t>.
- [20] O. Ilic, I. Kaminer, B. Zhen, O. D. Miller, H. Buljan, and M. Soljačić, *Science Advances* **3** (2017), 10.1126/sciadv.1602738.
- [21] M. Krger, T. Emig, G. Bimonte, and M. Kardar, *EPL (Europhysics Letters)* **95**, 21002 (2011).
- [22] R. Messina and M. Antezza, *Phys. Rev. A* **89**, 052104 (2014).
- [23] Y. Zheng and A. Ghanekar, *Journal of Applied Physics* **117**, 064314 (2015), <http://dx.doi.org/10.1063/1.4907913>.
- [24] B. Müller and M. Krüger, *Phys. Rev. A* **93**, 032511 (2016).
- [25] <https://homerreid.github.io/scuff-em-documentation>.
- [26] <https://homerreid.github.io/buff-em-documentation>.
- [27] M. T. H. Reid, J. White, and S. G. Johnson, *Phys. Rev. A* **88**, 022514 (2013).
- [28] A. W. Rodriguez, M. T. H. Reid, and S. G. Johnson, *Phys. Rev. B* **88**, 054305 (2013).
- [29] M. T. H. Reid, A. W. Rodriguez, J. White, and S. G. Johnson, *Phys. Rev. Lett.* **103**, 040401 (2009).
- [30] A. W. Rodriguez, M. T. H. Reid, J. Varela, J. D. Joannopoulos, F. Capasso, and S. G. Johnson, *Phys. Rev. Lett.* **110**, 014301 (2013).
- [31] L. D. Landau and E. Lifshitz, *Statistical Physics, Part 1* (Pergamon, 1980).
- [32] E. Lifshitz and L. Pitaevskii, *Statistical Physics, Part 2* (Pergamon, 1980).
- [33] H. B. G. Casimir and D. Polder, *Phys. Rev.* **73**, 360 (1948).
- [34] H. B. G. Casimir, *Koninkl. Ned. Adak. Wetenschap. Proc.* **51**, 793 (1948).
- [35] A. Lambrecht, A. Canaguier-Durand, R. Guérout, and S. Reynaud, in *Casimir Physics* (Springer, 2011) pp. 97–127.
- [36] F. Intravaia, P. S. Davids, R. S. Decca, V. A. Aksyuk, D. López, and D. A. R. Dalvit, *Phys. Rev. A* **86**, 042101 (2012).
- [37] S. Pasquali and A. C. Maggs, *Phys. Rev. A* **79**, 020102 (2009).
- [38] R. Messina, P. A. Maia Neto, B. Guizal, and M. Antezza, *Phys. Rev. A* **92**, 062504 (2015).
- [39] R. Gurout, C. Genet, A. Lambrecht, and S. Reynaud, *EPL (Europhysics Letters)* **111**, 44001 (2015).
- [40] M. Reid, A. Rodriguez, and S. Johnson, *Proceedings of the IEEE* **101**, 531 (2013).
- [41] J. D. Jackson, *Classical Electrodynamics*, 3rd ed. (John Wiley & Sons, 1999).
- [42] R. F. Harrington and J. L. Harrington, *Field Computation by Moment Methods*, 1st ed. (Oxford University Press, 1996).
- [43] W. Chew, M. Tong, and B. Hu, *Integral Equation Methods for Electromagnetic and Elastic Waves*, Synthesis Lectures on Computational Electromagnetics Series (Morgan & Claypool Publishers, 2009).
- [44] S. K. Volakis, John, *Integral Equation Methods for Electromagnetics* (SciTech Publishing, 2012).
- [45] M. T. H. Reid, J. White, and S. G. Johnson, *Phys. Rev. A* **84**, 010503 (2011).
- [46] S. Rao, D. Wilton, and A. Glisson, *Antennas and Propagation, IEEE Transactions on* **30**, 409 (1982).
- [47] D. Schaubert, D. Wilton, and A. Glisson, *Antennas and Propagation, IEEE Transactions on* **32**, 77 (1984).
- [48] S. Rytov, Y. Kravtsov, and V. Tatarskii, *Principles of Statistical Radiophysics* (Berlin: Springer, 1989).
- [49] D. Polder and M. Van Hove, *Phys. Rev. B* **4**, 3303 (1971).
- [50] M. Mishchenko, L. Travis, and A. Lacis, *Scattering, Absorption, and Emission of Light by Small Particles* (Cambridge University Press, 2002).
- [51] R. Cools, *Journal of Complexity* **19**, 445 (2003).
- [52] L. Landau, J. Bell, M. Kearsley, L. Pitaevskii, E. Lifshitz, and J. Sykes, *Electrodynamics of Continuous Media*, Course of Theoretical Physics (Elsevier Science, 2013).
- [53] P. W. Milonni, *The Quantum Vacuum: an Introduction to Quantum Electrodynamics* (Academic Press, 2013).
- [54] B. V. Derjaguin, *Scientific American* **203**, 47 (1960).
- [55] E. J. Moniz and D. H. Sharp, *Phys. Rev. D* **15**, 2850 (1977).
- [56] L. Landau, *The Classical Theory of Fields*, Course of Theoretical Physics (Elsevier Science, 2013).
- [57] A. Yaghjian, *Relativistic dynamics of a charged sphere: updating the Lorentz-Abraham model*, Vol. 11 (Springer Science & Business Media, 2008).
- [58] G. Ford and R. O’Connell, *Physics Letters A* **157**, 217 (1991).
- [59] D. J. Griffiths, T. C. Proctor, and D. F. Schroeter, *American Journal of Physics* **78** (2010).
- [60] K. S. Kunz and R. J. Luebbers, *The Finite Difference Time Domain Method for Electromagnetics* (CRC press, 1993).
- [61] J.-M. Jin, *The Finite Element Method in Electromagnetics* (John Wiley & Sons, 2014).
- [62] M. T. H. Reid and S. G. Johnson, *IEEE Transactions on Antennas and Propagation* **63**, 3588 (2015).
- [63] A. Polimeridis, M. Reid, S. Johnson, J. White, and A. Rodriguez, *Antennas and Propagation, IEEE Transactions on* **63**, 611 (2015).
- [64] M. T. H. Reid, J. K. White, and S. G. Johnson, *IEEE Transactions on Antennas and Propagation* **63**, 195 (2015).
- [65] W. C. Chew and W. C. Chew, *Waves and fields in inhomogeneous media*, Vol. 522 (IEEE press New York, 1995).
- [66] R. Collin, *Field Theory of Guided Waves*, IEEE/OUP series on electromagnetic wave theory (IEEE Press, 1991).
- [67] C. Tai, I. Antennas, P. Society, I. M. Theory, and T. Society, *Dyadic Green Functions in Electromagnetic Theory*, IEEE Press Series on Electromagnetic Waves (IEEE Press, 1994).
- [68] M. T. H. Reid, “Generalized Taylor-Duffy Method for Singular Tetrahedron-Product Integrals”, to appear.
- [69] E. Anderson, Z. Bai, C. Bischof, S. Blackford, J. Demmel, J. Dongarra, J. Du Croz, A. Greenbaum, S. Hammarling, A. McKenney, and D. Sorensen, *LAPACK Users’ Guide*, 3rd ed. (Society for Industrial and Applied Mathematics, Philadelphia, PA, 1999).

- [70] J. P. Boyd, *Chebyshev and Fourier spectral methods* (Courier Corporation, 2001).
- [71] J. A. Stratton and L. J. Chu, Phys. Rev. **56**, 99 (1939).
- [72] L. N. Medgyesi-Mitschang, J. M. Putnam, and M. B. Gedera, J. Opt. Soc. Am. A **11**, 1383 (1994).
- [73] C. F. Bohren and D. Huffman, *Absorption and Scattering of Light by Small Particles*, Wiley science paperback series (Wiley, 1983).
- [74] C. T. Tai and R. E. Collin, IEEE Transactions on Antennas and Propagation **48**, 1501 (2000).
- [75] T. Hansen and A. D. Yaghjian, *Plane-wave Theory of Time-Domain Fields* (IEEE Press, 1999).
- [76] P. A. M. Neto and H. M. Nussenzveig, EPL (Europhysics Letters) **50**, 702 (2000).
- [77] H. Gies and K. Klingmüller, Phys. Rev. Lett. **96**, 220401 (2006).
- [78] T. Emig, N. Graham, R. L. Jaffe, and M. Kardar, Phys. Rev. Lett. **99**, 170403 (2007).